THE ASTROPHYSICAL JOURNAL, 301:398–422, 1986 February 1

MOLECULAR CLOUDS AND STAR FORMATION IN THE INNER GALAXY: A COMPARISON OF CO, H II, AND FAR-INFRARED SURVEYS

P. C. MYERS,[1,2] T. M. DAME,[1] P. THADDEUS, AND R. S. COHEN
NASA/Goddard Institute for Space Studies

AND

R. F. SILVERBERG, E. DWEK, AND M. G. HAUSER
Laboratory for Extraterrestrial Physics, NASA/Goddard Space Flight Center
Received 1985 January 10; accepted 1985 July 29

ABSTRACT

We have compared surveys of the Galactic plane over $-1° \leq b \leq 1°$, $12° \leq l \leq 60°$, in the CO line at 2.6 mm, in the far-infrared (FIR) continuum at 150 μm and 250 μm, and in the radio continuum and H 110α recombination line at 6 cm. We identify 54 molecular cloud complexes, with mean mass $\sim 10^6\ M_\odot$. Most FIR sources are coincident with H II regions, and nearly all H II regions in turn are associated with molecular clouds. Clouds without H II regions tend to have lower mass than clouds with H II regions. The stellar content of a cloud is estimated by assuming that the associated FIR and radio continuum emission result from clusters whose mass distribution is the same as the initial mass function. The star formation efficiency (SFE) for the entire sample lies near 0.02, but some massive clouds are extremely star-poor, with SFE less than 10^{-3}. The stellar mass in a cloud appears correlated with the cloud mass, as $M_* \propto M_{\rm cloud}^{0.5\pm0.2}$. The mean gas density in a typical large complex is $\sim 20\ {\rm cm}^{-3}$ with volume filling fraction less than 0.1; the time to grow by accretion to this density is 10^7–10^8 yr. Presently visible inner Galaxy clouds have probably been forming stars of all types for less than 10^8 yr but may have been forming O stars for only the most recent $\sim 20\%$ of their lives.

Subject headings: galaxies: Milky Way — galaxies: structure — infrared: sources — interstellar: molecules — nebulae: H II regions — stars: formation

I. INTRODUCTION

The number and distribution of young stars in the inner Galaxy and the relation of young stars to their parent molecular clouds are of importance to the understanding of how molecular clouds evolve and form stars, in our Galaxy and in other galaxies. This subject has so far been approached from the somewhat separate viewpoints of molecular clouds (Dame *et al.* 1985; Sanders, Scoville, and Solomon 1985, and references therein), H II regions (Güsten and Mezger 1982, and references therein), and far-infrared (FIR) sources (Hauser *et al.* 1984, and references therein). These studies have revealed the large-scale distributions of molecular clouds, H II regions, and FIR sources in the inner Galaxy. However, detailed accounts of the associations among these objects and detailed estimates of the stellar content in each cloud remain to be made. Recently it has become possible to compare nearly complete surveys, with nearly identical angular resolution (8′–10′), over a significant part of the first quadrant. These are the CO $J = 1 \rightarrow 0$ line survey of Cohen *et al.* (1980), the 6 cm continuum surveys of Altenhoff *et al.* (1970, 1978), the associated H 110α line survey of Downes *et al.* (1980), and the FIR survey at 150, 250, and 300 μm of Hauser *et al.* (1984). This paper is a comparison of these surveys. Our main purposes are to determine the degree of association between FIR sources, H II regions, and molecular clouds in the first quadrant and to describe and analyze the stellar content of these molecular clouds. Our main conclusions are (1) most FIR sources coincide with H II regions, and nearly all H II regions coincide with molecular clouds; (2) the mass of stars in a cloud M_* is correlated with the cloud mass $M_{\rm cloud}$; (3) the star formation efficiency, SFE $\equiv M_*/(M_* + M_{\rm cloud})$, of all the molecular gas inferred from CO emission probably lies near 0.02; (4) the "infrared excess" of a source shows no significant decrease with galactocentric radius; and (5) clouds in the inner galaxy are probably several times 10^7 yr old and may have been producing O stars for only the most recent $\sim 20\%$ of their lives.

The method used here, combining FIR and radio continuum luminosity to estimate the stellar content of a cloud, is fairly general and may be extended to other parts of the Galaxy, and to other galaxies, with better data. It should also prove possible to increase greatly the accuracy of the present stellar content estimates by using high-resolution, high-sensitivity data from the *IRAS* satellite.

The data used in this paper are described in § II, the criteria of association are developed, tested, and used in §§ III and IV, the source luminosities are calculated in § V, and the stellar mass and star formation efficiencies are estimated in § VI. The results are discussed and interpreted in § VII and are summarized in § VIII.

II. DATA

The data used in this paper are based on the first-quadrant surveys summarized in Table 1. The surveys were chosen so as to permit comparison of information based on FIR, radio continuum, and CO observations with similar coverage, sampling, and angular resolution, and with the best sensitivity available. It is instructive to compare relatively unprocessed maps in Figure 1 from surveys 1, 2, and 5 before proceeding to more detailed analysis. These maps cover $25° \leq l \leq 35°$,

[1] NAS-NRC Resident Research Associate.
[2] Visiting Scientist, Harvard-Smithsonian Center for Astrophysics.

TABLE 1

SURVEYS OF THE FIRST QUADRANT OF THE GALACTIC PLANE

Type of Emission	λ	Angular Resolution	Velocity Resolution (km s^{-1})	Sensitivity	Sampling	Reference
FIR continuum	150 μm	10′	...	350 Jy $Hz^{-1/2}$	Continuous	1
	250 μm		...	270 Jy $Hz^{-1/2}$		
	300 μm		...	190 Jy $Hz^{-1/2}$		
Radio continuum	6 cm	11	...	4 Jy	Continuous	2
	6 cm	2.6	...	0.01 K	Continuous	3
H 110α line	6 cm	2.6	1.9	0.03 K	Peaks of No. 3 with flux density > 1 Jy	4
CO $J = 1 \rightarrow 0$ line	2.6 mm	8	0.65	0.6 K	Every 7.5 or every 15′	5

NOTE.—All surveys have common coverage in the region $12° \leq l \leq 60°$, $-1° \leq b \leq 1°$.

REFERENCES.—(1) Hauser *et al.* 1984. (2) Altenhoff *et al.* 1970. (3) Altenhoff *et al.* 1978. (4) Downes *et al.* 1980. (5) Cohen *et al.* 1980 and Cohen, Dame, and Thaddeus 1985.

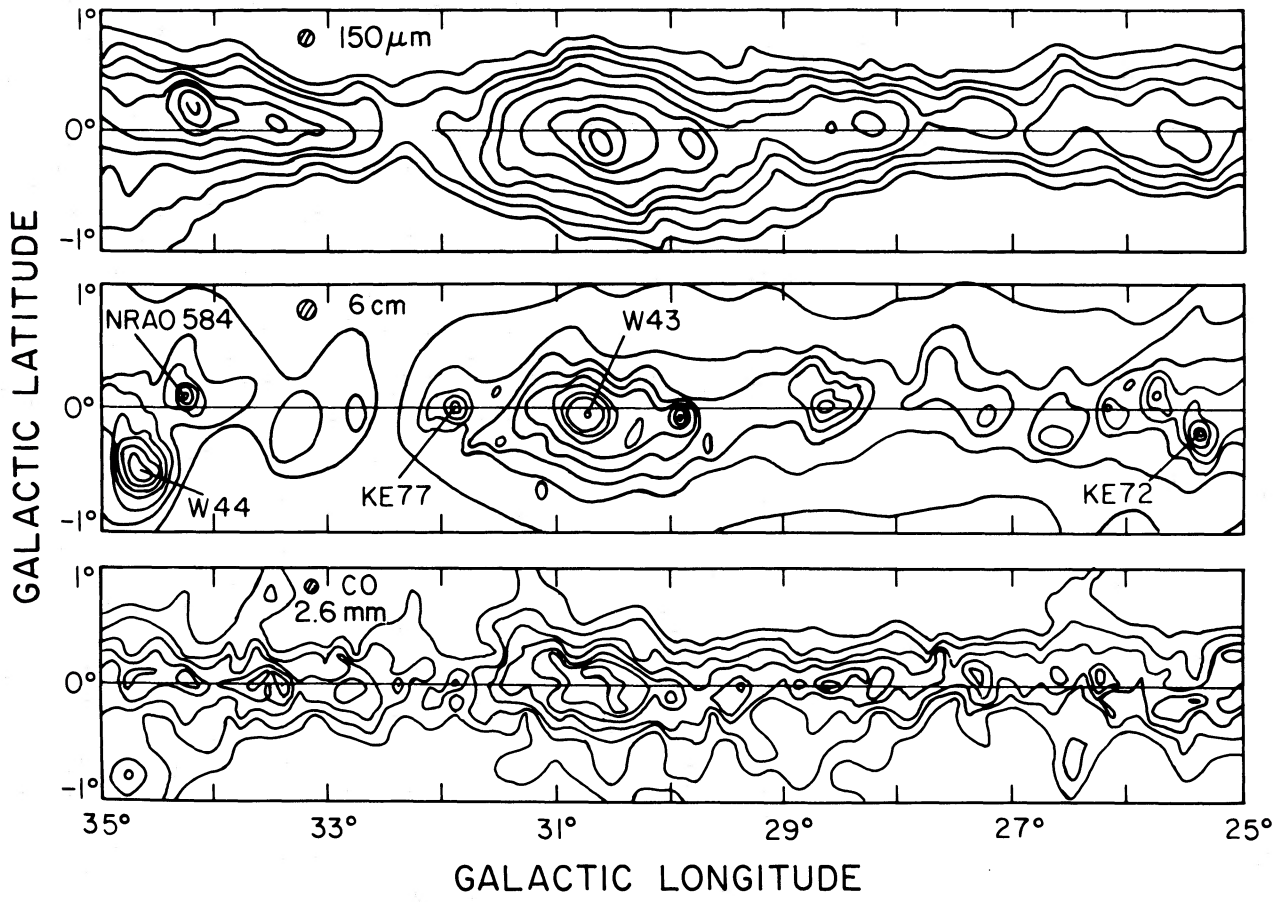

FIG. 1.—Comparison of three surveys of the Galactic plane over the latitude range $-1° \leq b \leq 1°$ and longitude range $25° \leq l \leq 35°$. (*top*) 150 μm continuum emission (Hauser *et al.* 1984), with contours representing 1.0, 2.0, 3.0, 4.0, 5.5, 7.0, 9.0, 11, 15, 19, 25, 33, 44, 60, 76, and 100 times 2.9×10^{-11} W m^{-2} in the beam. (*middle*) 6 cm continuum emission (Altenhoff *et al.* 1970), with contours increasing uniformly in integer multiples of 0.23 K brightness temperature. (*bottom*) 2.6 mm $J = 1 \rightarrow 0$ ^{12}CO line emission, integrated over all Doppler velocities allowed by Galactic rotation, with contours increasing in integer multiples of 26 K km s^{-1}, starting from 78 K km s^{-1}.

TABLE 2

FIRST-QUADRANT[a] MOLECULAR CLOUDS AND THEIR ASSOCIATED H II REGIONS AND FAR-INFRARED SOURCES

MOLECULAR CLOUD					H II REGION				FIR SOURCE			
Name (1)	l_{min} (2)	l_{max} (3)	D (kpc) (4)	log M_{cloud} ($M_\odot$) (5)	l (6)	b (7)	V_{LSR} (km s^{-1}) (8)	log L(Lyα) ($L_\odot$) (9)	l (10)	b (11)	log L(FIR) ($L_\odot$) (12)	Note (13)
12,45	12°0	13°5	5.3	6.5	12°8	− 0°3	37	5.62	12°9	− 0°2	6.3	
13,54	12.0	15.0	5.8	5.9	13.1	+ 0.0	54	4.85	13.3	+ 0.0	...	b
14,20	12.0	15.7	2.3	6.0	14.5	− 0.6	11	3.69	14.3	− 0.5	...	b
					15.1	− 0.6	17	6.30	15.0	− 0.7	6.6	M17
14,39	13.5	15.5	4.4	6.2	13.9	+ 0.3	53	4.52	13.9	+ 0.0	...	b, c
					14.0	− 0.1	31	4.44	13.9	− 0.2	...	b
					14.6	+ 0.0	37	5.59	14.5	+ 0.0	6.5	d
17,22	15.6	18.5	2.0	5.5	17.0	+ 0.9	24	4.78	17.1	+ 0.8	6.1	M16
17,44	15.5	17.5	4.4	6.2	16.4	− 0.3	44	3.94	16.3	− 0.2	6.4	e
17,58	15.0	17.5	5.3	5.8	...	...	...	<4.1	...	...	...	
18,48	17.5	19.7	4.4	6.1	18.3	− 0.3	48	5.11	18.2	− 0.3	5.7	S53
					19.0	+ 0.0	50	4.32	19.0	− 0.1	5.4	
					19.6	− 0.3	40	4.70	19.7	− 0.2	...	b
19,65	17.5	20.3	5.5	6.3	18.9	− 0.5	67	5.61	...	...	...	b, f
					19.1	− 0.3	61	4.95	...	...	...	b, f
20,25	18.5	23.5	2.5	5.1	19.5	+ 0.1	24	5.14	19.4	+ 0.0	...	b
					21.0	+ 0.1	18	3.49	...	...	...	b, f
20,42	19.7	21.2	3.8	5.6	20.1	− 0.1	46	3.86	...	...	...	b, f
21,60	20.3	21.2	14	6.3	20.8	− 0.1	57	6.06	20.6	− 0.3	6.6	
22,53	21.2	23.3	4.4	6.2	...	...	...	<3.9	...	...	...	
23,78N	19.5	24.8	5.9	6.4	...	...	...	<4.2	...	...	...	
23,78F	19.5	24.8	12.6	7.0	22.8	− 0.5	74	5.32	22.9	− 0.3	...	b, g
					23.0	− 0.4	78	5.71	22.9	− 0.3	...	b, g
					23.9	− 0.1	75	4.93	23.9	+ 0.1	...	b, g
					24.0	+ 0.1	80	5.28	23.9	+ 0.1	...	b, g
24,42	23.2	25.5	3.4	5.6	25.3	+ 0.3	45	3.65	...	...	...	b, f
24,98	20.8	26.6	7.1	6.9	23.4	− 0.3	104	5.41	23.3	− 0.2	6.9	g
					23.5	+ 0.0	91	5.41	23.3	− 0.2	6.9	g
					24.5	− 0.3	96	5.56	...	...	...	b, g
					24.5	+ 0.5	102	5.65	...	...	...	b, g
					24.8	+ 0.1	107	5.18	24.8	+ 0.1	5.9	
					25.8	+ 0.3	112	5.87	...	...	...	b, f
					26.5	+ 0.4	90	5.23	...	...	...	b, f
24,110	22.0	26.0	9	6.4	24.5	+ 0.3	117	5.66	24.4	+ 0.1	5.4	
25,55N	23.4	26.0	4.1	6.0	...	...	...	<3.9	...	...	...	
25,55F	23.4	26.0	14	6.6	25.4	+ 0.1	59	6.22	25.4	− 0.2	7.4	
26,65	26.0	27.0	4.9	5.5	...	...	...	<4.0	...	...	...	
27,25	26.0	28.0	16	6.2	...	...	...	<5.1	...	...	...	
27,34	26.4	29.5	15	6.5	26.1	− 0.1	33	5.61	26.2	+ 0.0	6.4	
					27.3	+ 0.1	33	5.07	27.2	+ 0.0	...	b
					27.5	+ 0.1	36	5.47	...	...	...	b, f
29,52	27.5	30.5	3.8	5.4	...	...	...	<3.8	...	...	...	
29,80	27.0	31.8	5.7	6.7	31.4	− 0.3	90	4.44	...	...	...	b, f
31,12	31.0	31.5	0.9	3.2	...	...	...	<5.1	...	...	...	
31,48	29.5	32.9	14	6.6	...	...	...	<4.9	...	...	...	
31,95	26.6	34.8	6.9	7.0	28.6	+ 0.0	96	5.39	28.6	+ 0.0	...	b
					30.0	+ 0.0	99	5.56	29.8	− 0.1	6.0	
					30.3	− 0.1	99	4.68	...	...	...	b, f
					30.8	+ 0.0	90	6.14	30.6	− 0.2	7.0	W43
					31.1	+ 0.0	99	4.71	...	...	...	b, f
					31.4	+ 0.3	104	4.47	...	...	...	b, f
					33.9	+ 0.1	98	4.42	...	...	...	b, f
33,10	32.5	32.9	16	6.0	32.8	+ 0.3	17	5.54	32.7	+ 0.2	...	b
35,13	32.9	35.5	0.9	4.6	...	...	...	<2.6	...	...	...	L617
35,44	33.0	36.5	3.1	5.8	35.0	− 0.5	52	3.83	...	...	...	b, f, h
35,44+	31.0	35.5	3.1	5.7	34.3	+ 0.1	53	4.68	34.2	+ 0.2	6.0	W44, h
					35.6	+ 0.0	52	4.53	35.5	+ 0.1	5.0	
36,57	35.5	37.5	12	6.7	37.4	+ 0.0	60	5.59	...	...	...	b, f
37,82	31.8	40.5	9.5	7.0	...	...	...	<4.6	...	...	...	b, f
38,16	37.0	40.0	1.0	4.5	39.3	+ 0.0	24	2.95	...	...	...	b, f
39,32	38.0	40.0	2.2	5.0	...	...	...	<3.3	...	...	...	b, f, i
39,42	38.5	39.5	2.9	4.7	...	...	...	<3.6	...	...	...	b, f, j
40,59	37.6	40.7	11	6.8	37.9	− 0.4	60	5.39	37.7	− 0.3	6.3	
41,37	40.6	42.3	2.6	5.1	...	...	...	<3.5	...	...	...	b, f
42,16	41.4	42.1	14	5.8	41.5	+ 0.0	15	5.15	...	...	...	b, f
43,11	42.9	43.4	14	5.6	43.1	+ 0.0	10	6.64	43.2	+ 0.0	7.9	W49, k
43,11+	42.9	43.4	14	5.5	...	...	...	...	...	...	...	k
43,63	40.7	43.5	10	6.7	41.1	− 0.3	58	5.34	41.0	− 0.2	6.2	l
					42.1	− 0.6	66	5.04	...	...	...	b, f
					43.1	− 0.5	56	4.65	...	...	...	b, f

TABLE 2—*Continued*

Molecular Cloud					H II Region				FIR Source			
Name (1)	l_{min} (2)	l_{max} (3)	D (kpc) (4)	log M_{cloud} ($M_\odot$) (5)	l (6)	b (7)	V_{LSR} (km s^{-1}) (8)	log L(Lyα) ($L_\odot$) (9)	l (10)	b (11)	log L(FIR) ($L_\odot$) (12)	Note (13)
43,63+	40.°7	43.°5	10	5.4	...	...	...	<4.6	...	...	...	b, f, l
44,60	43.5	44.7	9.6	6.2	...	...	...	<4.6	...	...	...	b, f
46,25	45.0	46.5	1.8	4.2	...	...	...	<3.2	...	...	...	b, f
46,59	44.7	47.2	9.2	6.5	45.°1	+ 0.°1	58	5.32	...	...	...	b, f
					45.5	+ 0.1	54	5.57	45.°5	+ 0.°1	6.3	
					46.5	− 0.3	57	5.28	...	...	...	b, f
49,18	48.5	49.0	12	5.6	48.6	+ 0.0	18	5.68	48.8	+ 0.1	7.3	
49,59	48.5	50.2	7.3	6.2	48.9	− 0.3	66	5.44	...	...	...	b, f
					49.2	− 0.3	67	5.68	...	...	...	b, f
					49.5	− 0.4	59	6.41	49.6	− 0.3	6.4	W51
					50.1	− 0.6	70	4.69	...	...	...	b, f
50,45	48.5	51.0	3.6	5.4	...	...	...	<3.8	...	...	...	b, f
51,55	50.8	51.8	5.0	5.6	51.4	+ 0.0	53	4.56	51.3	+ 0.0	...	b
53,24	52.6	54.0	1.9	4.6	...	...	...	<3.2	...	...	...	b, f
53,60	51.8	53.3	3.4	5.0	...	...	...	<3.7	...	...	...	b, f
54,40	53.8	54.3	8.3	5.3	54.1	− 0.1	43	4.85	54.1	+ 0.0	5.2	
56,36	55.0	57.2	5.6	5.7	...	...	...	<4.1	...	...	...	b, f
58,37	57.2	59.4	3.9	5.2	...	...	...	<3.8	...	...	...	b, f
60,27	58.7	60.0	2.6	4.9	...	...	...	<3.5	...	...	...	b, f
Median	...	...	...	5.8	...	...	...	5.28	...	...	6.3	

[a] In the Galactic coordinate range $12° \le l \le 60°$, $-1° \le b \le 1°$. Each cloud is named with the l, v coordinates of its peak on the l-v diagram.
[b] Not detected or very weak at 250 μm.
[c] V_{LSR} of H II region exceeds that of CO cloud by more than the adopted limit of 10 km s^{-1}, but H II region position agrees well with that of CO peak.
[d] FIR source 14.5 + 0.0 has an unusually high temperature (46 K) deduced from the FIR data according to the methods used in this paper. Consequently the derived luminosity, $10^{6.5}$ $L_\odot$, may be an overestimate.
[e] L(Lyα) is remarkably low for a FIR source of the deduced L(FIR).
[f] Not detected or very weak at 150 μm.
[g] Double FIR identification.
[h] Log [M_{cloud}(35,44) + M_{cloud}(35,44+)] = 6.1.
[i] Cloud latitude boundaries $-0.°15 \le b \le 1°$.
[j] Cloud latitude boundaries $-1° \le b \le -0.°15$.
[k] Log [M_{cloud}(43,11) + M_{cloud}(43,11+)] = 5.9.
[l] Log [M_{cloud}(43,63) + M_{cloud}(43,63+)] = 6.7.

$-1° \le b \le 1°$, in the 150 μm FIR (Hauser *et al.* 1984), in the 6 cm radio continuum (Altenhoff *et al.* 1970), and in the 2.6 mm CO line (Cohen *et al.* 1980). The CO map is integrated over a window including all velocities permitted by Galactic rotation, to allow direct comparison with the two continuum surveys. The designation of the most prominent radio continuum sources is that given in Table 2 of Altenhoff *et al.* (1970).

As in earlier comparisons (e.g., Okuda 1981), these maps show that the radio continuum sources have smallest angular size, least "background," and best definition. The FIR sources are well correlated with the radio continuum sources but are more extended and sit on a bright "diffuse background." The CO emission shows some correspondence with the main FIR and radio continuum structures. But since the CO maps are integrated over wide velocity windows, line blending degrades cloud definition compared to that obtained from narrow windows, as in § IV*a*. To the extent that CO regions can be resolved, each typically "encloses" several radio continuum and FIR sources. The correlation in position between radio continuum peaks and FIR peaks appears good; and while radio continuum/FIR peaks are seen where CO emission is present, their correlation with CO peaks is poorer.

III. ASSOCIATION OF H II REGIONS AND FAR-INFRARED SOURCES

a) Position-Velocity Map of H II *Regions*

To compare H II regions with FIR sources and molecular clouds, we have sought to improve on simple continuum maps such as those of Altenhoff *et al.* (1970), because (1) they contain numerous nonthermal sources (supernova remnants and quasars); (2) their sensitivity, ~4 Jy, is poor compared to that of modern surveys; and, most important, (3) they contain no velocity information. Therefore we have used sources in the range $-1° < b < 1°$, $12° < l < 60°$ that were detected in the H 110α line survey by Downes *et al.* (1980), to create a synthetic "position-velocity" map of H II regions. The continuum emission from each source was represented by a circularly symmetric Gaussian, with center position, FWHM diameter, and peak intensity as given in Table II of Downes *et al.* (1980). The velocity distribution of emitting gas was also assumed to be Gaussian. At each position within the source, the center velocity and FWHM velocity width were taken to be the center velocity and FWHM of the H 110α line measured by Downes *et al.* (1980) at the peak of the source. This three-dimensional map, based on observations made with a 2.′6 FWHM beam, was gridded at 1.′0 intervals in l and b and at 0.65 km s^{-1} intervals in v_{LSR} and was then convolved in l and b with a Gaussian having 8′ FWHM, in order to facilitate comparison with the Cohen *et al.* (1980) CO survey (8′ beam) and the Hauser *et al.* (1984) FIR survey (10′ beam). The resulting map is ~36 times more sensitive to a point source, and contains ~50% more thermal sources, than that of Altenhoff *et al.* (1970), when identical areas of coverage are compared.

There are 68 distinct sources in this synthetic map. Their peak positions, integrated fluxes, and peak velocities are listed in Table 2. Where comparison is possible, these source par-

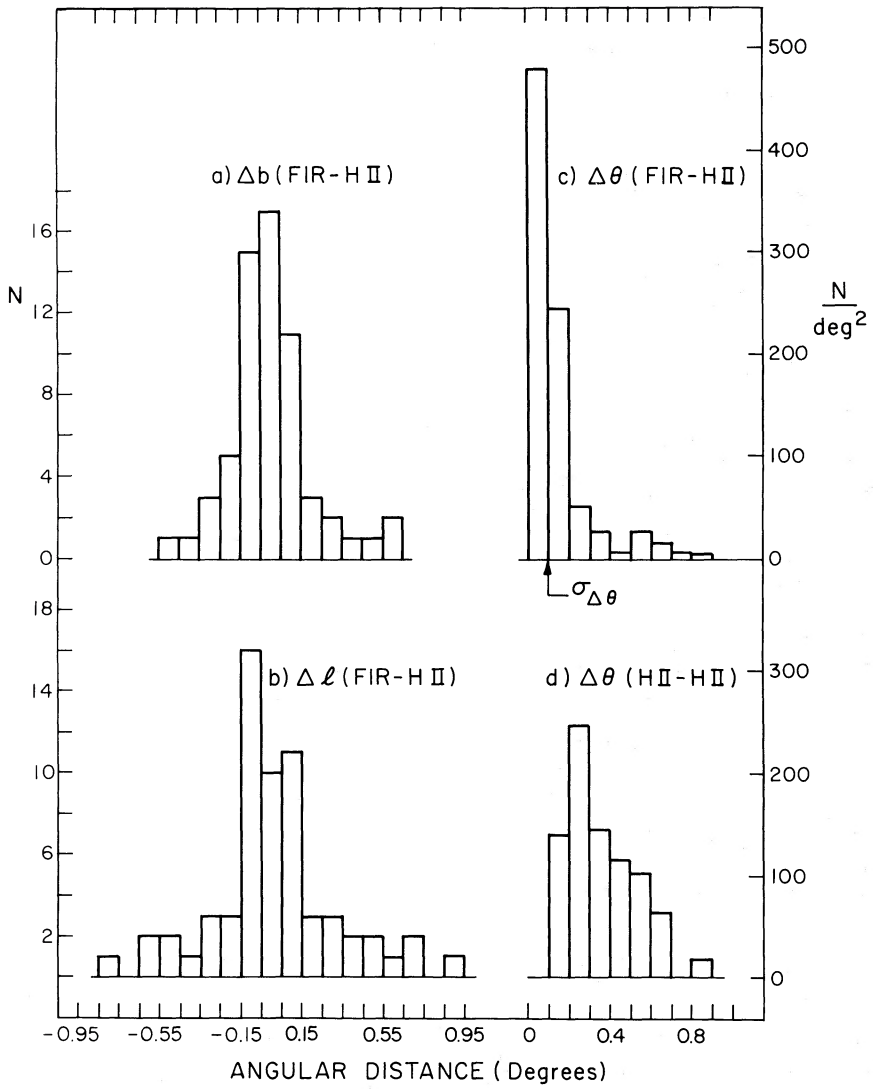

FIG. 2.—Distributions of relative angular position between FIR sources from Hauser *et al.* (1984) and H II regions in the smoothed map described in § IIIa. (*a*) Number vs. Δb(FIR–H II), the Galactic latitude distance from each FIR source to the nearest H II region. (*b*) Number vs. Δl(FIR–H II), the Galactic longitude distance from each FIR source to the nearest H II region. (*c*) Number per square degree vs. $\Delta\theta$(FIR–H II), the absolute angular distance from each FIR source to the nearest H II region. (*d*) Number per square degree vs. $\Delta\theta$(H II–H II), the absolute angular distance from each H II region to its nearest neighbor.

ameters are in good agreement with those of the 41 H II regions found in the same *l*-*b* range in the less sensitive H 109α line survey by Reifenstein *et al.* (1970).

b) Relative Positions of H II *Regions and Far-infrared Sources*

To aid in the choice of a criterion of association between H II regions and FIR sources, we present in Figure 2 four histograms of relative angular position. For the 63 FIR source peaks having $-1° \leq b \leq 1°$, $12° \leq l \leq 60°$ in Hauser *et al.* (1984), we plot histograms of (*a*) Δb(FIR–H II), the Galactic latitude distance to the nearest H II region peak in the synthetic H II region map; (*b*) Δl(FIR–H II), the Galactic longitude distance to the nearest H II region peak; (*c*) $\Delta\theta$(FIR–H II), the absolute angular distance to the nearest H II peak; and (*d*) $\Delta\theta$(H II–H II), the absolute angular distance from each H II region peak to that of its nearest neighbor.

Figures 2*a* and 2*b* show that the histograms are approximately symmetrical about zero offset, as expected if pointing and other position errors are randomly distributed. A vertical line in Figure 2*c* at 0°.1 represents the estimated 1 σ uncertainty in $\Delta\theta$(FIR–H II) due to the pointing uncertainty in the FIR observations (Hauser *et al.* 1984) and to the effects of gridding the H II region map at 0°.125 intervals. The histogram falls off sharply for offsets greater than this uncertainty, suggesting that most of the nearest-in-angle FIR–H II pairs are in fact coincident within position errors. Some of these coincidences may be due to chance rather than physical association, but comparison of Figures 2*c* and 2*d* suggests that chance coincidence must be rare. If the relative positions of FIR sources and H II regions were uncorrelated, histogram (*c*) would peak at an angular distance about half the characteristic spacing between H II regions. Histogram (*d*) shows that the typical spacing between H II regions is about 0°.4, while (*c*) peaks at a value less than 0°.1.

Therefore, the nearest H II region to a FIR source is generally associated, and it remains to limit the acceptable position offsets to a reasonable range. For this purpose we adopt 0°.30,

about 3 σ, as the maximum value of $\Delta\theta$(FIR–H II) for association. This choice leads to the rejection of 24 nearest neighbors as not associated, about one FIR–H II pair out of three. This fraction is essentially the same as that found by Hauser *et al.* (1984) in comparing their FIR sources with the 6 cm sources of Altenhoff *et al.* (1970). The typical FIR source without an associated H II region is distinctly weaker than the typical FIR source with an associated H II region, the mean 150 μm flux density being $2.1 \pm 0.2 \times 10^3$ Jy as opposed to $4.1 \pm 0.4 \times 10^3$ Jy. Therefore some of the FIR sources without H II regions may be due to stars later than type O. This point warrants further investigation.

IV. ASSOCIATION OF CO CLOUDS AND H II REGIONS

a) Processed CO *Maps*

Figure 1 shows that the ability of CO maps to delineate molecular clouds is largely lost when the CO data of Cohen *et al.* (1980) are treated like continuum maps and are integrated over the entire frequency window of the spectrometer. This arises mainly because of (1) confusion and blending of lines from two or more clouds along the same line of sight, and (2) the presence of a "background" of weak emission extended over angular and velocity dimensions bigger than that of individual clouds with strong ($T_A^* \approx 10$ K), narrow ($\Delta V \approx 5$ km s^{-1}) lines. Since the CO line emission has relatively narrow bandwidth, we filter out the background in the standard way by integrating the CO emission over velocity windows, each only a few line widths wide. The choice of window width is a compromise: narrow (~ 10 km s^{-1}) windows give excellent cloud definition but cause clouds with large velocity gradients to be spread over several maps with adjacent velocity windows; broad (~ 30 km s^{-1}) windows allow most clouds to appear only once but blend distinct velocity features together and give poor cloud definition. We adopt windows 20 km s^{-1} wide, a value typical of those used by Dame *et al.* (1985). To cover the range of emission velocities 0–120 km s^{-1} with contiguous 20 km s^{-1} windows we made *l-b* maps with the windows of V_{LSR} centered at odd multiples of 10 km s^{-1}, i.e., 10, 30, ..., 110 km s^{-1}.

In a 20 km s^{-1} spectral window, the velocity-integrated "background" line emission is sometimes comparable to the velocity-integrated "cloud" line emission, so we have clipped the data to further improve cloud definition. All intensities below 2 K were set to zero before integrating over the velocity windows, as was done by Dame *et al.* (1985) in preparing their Figure 7. The reduced cloud mass depends on the chosen threshold: as the threshold increases from 1.5 to 2.5 K, the average cloud mass decreases by about 60%. However, 2 K is a reasonable threshold choice. For thresholds less than ~ 1 K, confusion significantly reduces cloud definition. For thresholds more than ~ 3 K, small clouds are lost. For simplicity, a constant 2 K threshold was used over the entire angular area of the map, even though the CO background is significantly larger below $l = 30°$ than above. Therefore the masses of clouds with $l < 30°$ may be overestimated, and the masses of clouds with $l > 30°$ may be underestimated, by a typical factor of 2, in comparison to masses estimated from a regionally varying threshold.

Maps of the CO emission with clipping and velocity integration as described above are presented in Figures 3*a* and 3*b*.

b) Classification, Distances, and Masses of CO *Clouds*

The emission shown in Figure 3 has been divided into 52 discrete emission features; two of these are judged to be line-of-sight blends, so that 54 discrete "clouds" result. An emission feature is classified as a cloud if it appears as a local maximum of emission on both the *l-v* diagram (integrated over *b*) and on Figure 3. The *l-v* diagram (not shown here) is an unsmoothed version of Figure 3 of Dame *et al.* (1985); the two differ only slightly. A boundary between clouds, indicated as dashes in Figure 3, was usually drawn through the deepest local minima between features; in several cases its position was influenced by the appearance of the features on the *l-v* diagram. In some cases the location of a boundary line is arbitrary (e.g., between clouds 24,98 and 31,95), and relative uncertainty of a factor of ~ 2 in the cloud dimension perpendicular to the boundary line results. This leads to relative uncertainty of a factor of ~ 2 in mass and $\sim 2^{1/2}$ in mean number density. However, these errors have little influence on the main conclusions of this paper.

More significant changes in cloud properties arise if the number of boundary lines in Figure 3 is increased appreciably. For example, suppose a structure we call a "cloud" contains S local maxima of integrated intensity, and their individual properties are to be analyzed.[3] Then these units, if identical, will have size, mass, and density that are multiples of those estimated here by respective factors $\sim S^{-1/2}$, $\sim S^{-1}$ and $\sim S^{1/2}$. In § VII*a* we compare cloud statistics from this paper with those of Sanders, Scoville, and Solomon (1985), whose method of identifying clouds resembles the alternative described here, and we find that typically $S \approx 5$. This alternate cloud definition can thus lead to a reduction of order 5 in cloud mass from that used here, and this reduction is comparable to the random uncertainty in the mass estimate (§ VI*d*).

The cloud estimates presented here are, we believe, most appropriate to describing the largest associated structures, with relative mass uncertainties of order ~ 2 due to uncertainty in placement of boundary lines. This choice is supported by the close agreement between CO–based mass and virial mass described by Dame *et al.* (1985). Cloud estimates based on one local maximum per cloud tend to give the smallest possible mass and size consistent with the data and take no account of the tendency of such maxima to occur in coherent large structures, demonstrated recently by Rivolo, Solomon, and Sanders (1985). Nonetheless, we note throughout this paper how this change in definition would modify our conclusions. In most cases, there is no significant change.

Each cloud is named, and labeled in Figure 3, with the (l, v)-coordinates of its peak in the *l-v* diagram. Occasionally a cloud appears to straddle two adjacent velocity windows, having two emission features at approximately the same range of l. Then we denote the more prominent feature as l, v and the less prominent feature as l, $v+$ (l, $v-$) if the less prominent feature is higher (lower) in velocity. Generally, small, isolated features with only one or two contours were not cataloged as clouds, except if they occur in the lowest velocity (10–30 km s^{-1}) window. In that case, they may represent clouds with significant mass if they lie at the far kinematic distance (e.g., the cloud 43,11 associated with W49).

The distance to all but two clouds was obtained by applying

[3] The present method of assigning boundaries estimates the largest associated structures. For simplicity, we term them "clouds," although one might also call them "complexes" that contain "clouds" or "clumps."

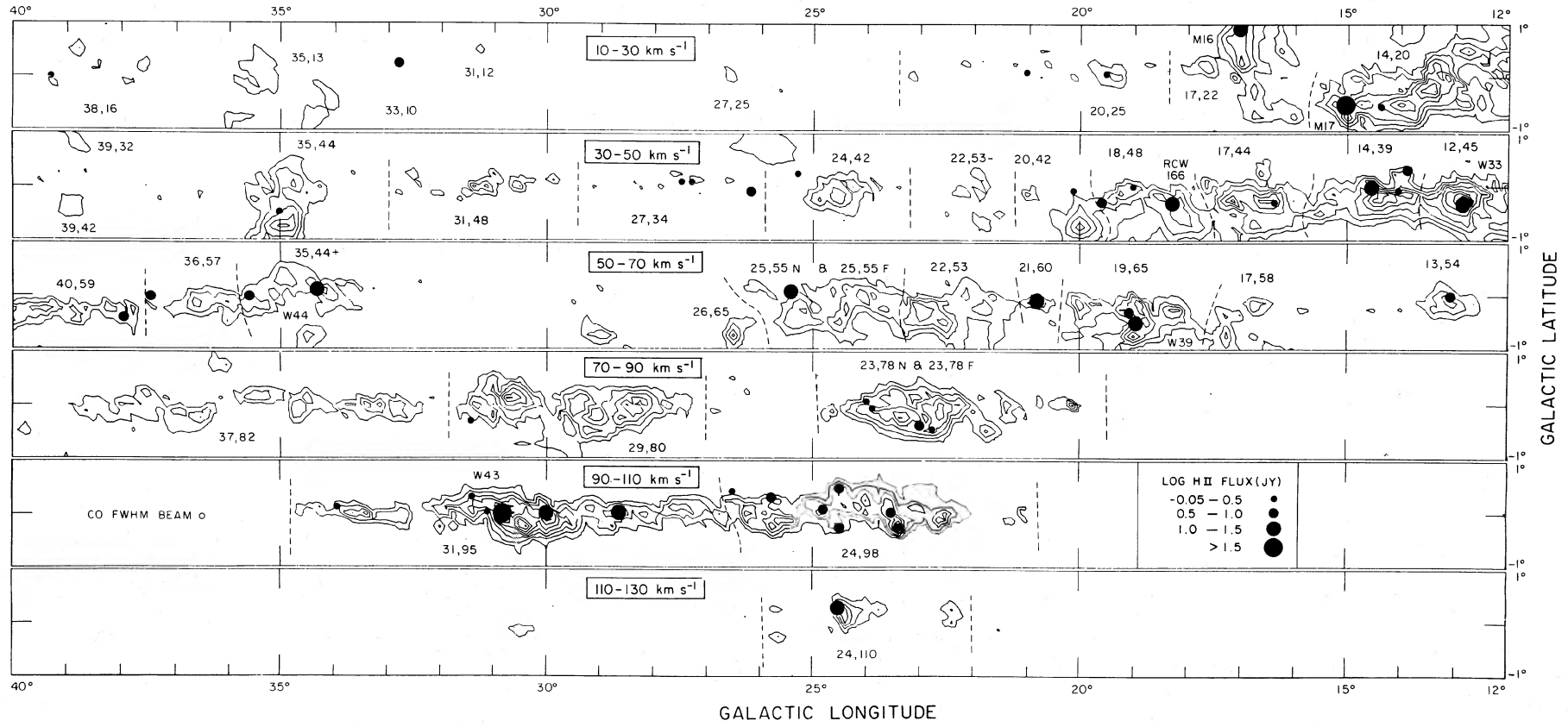

FIG. 3a

FIG. 3.—Longitude-latitude maps of CO emission, based on the data of Cohen *et al.* (1980). In each map, the CO data have been clipped at 2 K and then integrated over a velocity interval 20 km s^{-1} wide. The velocity range of each map is given in a rectangular box near the center of the map. (*a*) For $12° \leq l \leq 40°$, $-1° \leq b \leq 1°$, the contours increase uniformly in integer multiples of 14.2 K km s^{-1}. (*b*) For $40° \leq l \leq 60°$, $-1° \leq b \leq 1°$, the contour intervals are as in (*a*), except that a lower contour at 7.1 K km s^{-1} has been added to bring out weak emission structure. Maps with $40° \leq l \leq 60°$, $-1° \leq b \leq 1°$ for 90–110 km s^{-1} and 110–130 km s^{-1} are blank and therefore have been omitted.

In each map, filled circles represent the (l, b)-position and recombination line velocity of H II regions associated with the molecular clouds. The size of the circle indicates the 6 cm continuum flux density, as shown in the insets. Each cloud is labelled with the (l, v)-coordinates of peak cloud emission on the l-v diagram. Dashed lines indicate boundaries adopted for estimating cloud masses.

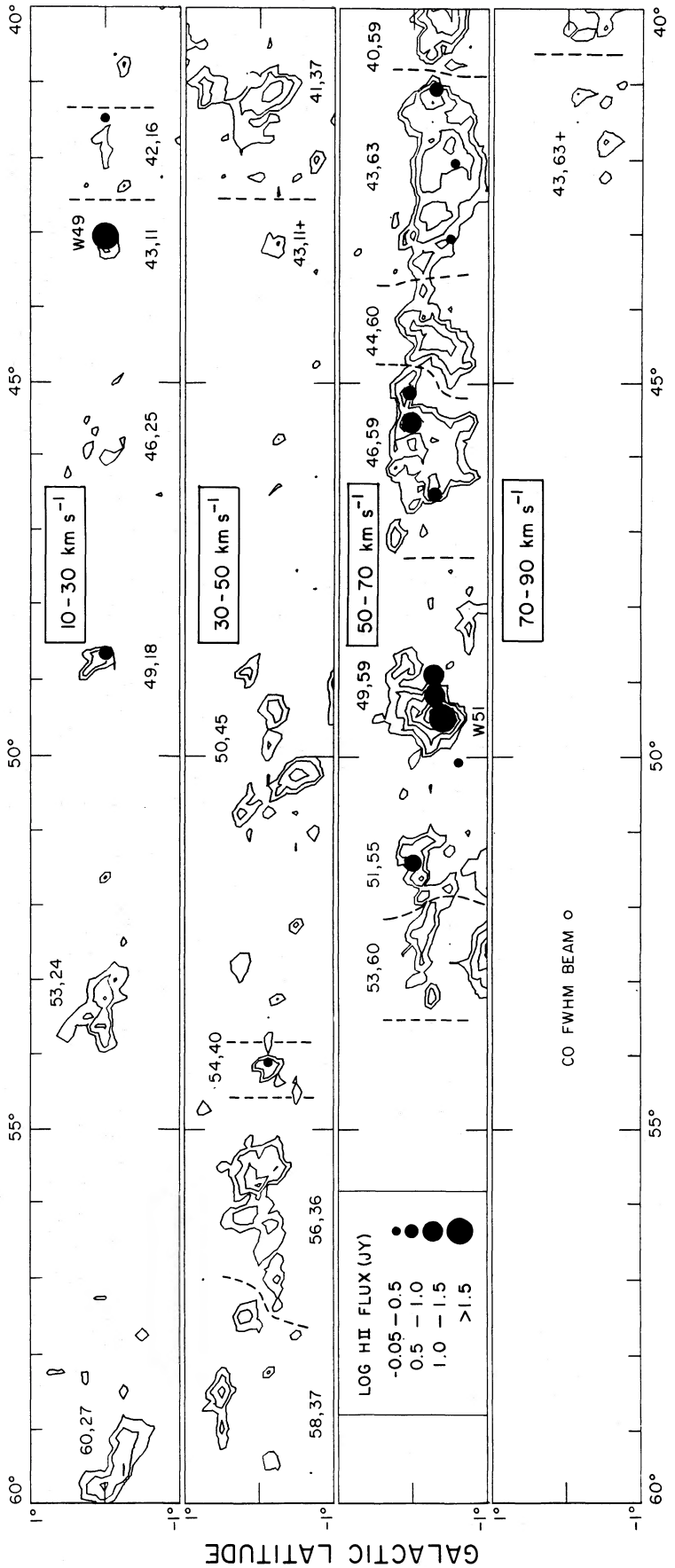

FIG. 3b

the rotation curve expression of Burton (1971), which agrees well with that of Schmidt (1965). The near-far ambiguity was resolved by using the velocity of H_2CO line absorption (Downes *et al.* 1980) or the latitude extent of the cloud (Dame *et al.* 1985). For M16 and M17, the distance from optical spectrophotometry was adopted.

The mass $M_{\rm cloud}$ of each cloud in Figure 3 was estimated by integrating the emission over the l- and b-limits indicated by the dashed cloud boundaries. We used the relation derived by Lebrun *et al.* (1983) from an intercomparison of CO, H I, and diffuse γ-ray emission in the first quadrant:

$$N_{\rm H_2}(l, b) = 2 \times 10^{20} \int T_{12}(l, b, v) dv \ {\rm cm}^{-2} , \qquad (1)$$

where $N_{\rm H_2}$ is the column density of H_2 molecules and T_{12} is the brightness temperature of the ^{12}CO line emission. We assumed one helium atom for every five hydrogen molecules. In simple models of cloud geometry, integration over the line profile as in equation (1) would be expected to underestimate the column density for optically thick lines such as the 2.6 mm line of ^{12}CO. However, a wide range of independent investigations supports the use of this method (Liszt 1982), and cloud masses estimated in this way agree closely with virial estimates (Dame *et al.* 1985).

The name, boundaries, adopted distance, and mass of each CO cloud are summarized in Table 2. For each associated H II region, Table 2 gives the coordinates of peak emission on the 6 cm map described in § III*a*, the $V_{\rm LSR}$ of the H 110α line; and the Lyman-alpha luminosity (§ V*b*). For each FIR source associated with an H II region, Table 2 gives the coordinates of peak 150 μm emission (Hauser *et al.* 1984) and the source luminosity, after subtraction of an appropriate "background" (Appendices B, C). Each cloud is described further in Appendix A, which notes prominent associated H II regions, the basis for distance determination, information about the choice of cloud boundaries, and other properties deserving comment.

The total mass in this sample is $1.1 \times 10^8 \ M_\odot$, and the mean and standard deviation in cloud mass are $1.9 \times 10^6 \ M_\odot$ and $2.5 \times 10^6 \ M_\odot$ respectively. The distribution of masses (uncorrected for beam dilution of distant clouds) resembles those found by Dame *et al.* (1985) and Sanders, Solomon, and Scoville (1983), in that most of the mass is in relatively few massive clouds. The mass uncertainties include factors of ~ 2 in conversion between CO and H_2 mass, in the choice of clipping threshold, and occasionally in the choice of cloud boundary. There may also be a bias of a similar factor, associated with background removal by clipping as opposed to subtraction. The ratio of cloud mass, as deduced here, to that of Dame *et al.* (1985) is typically 1.5–2.0, depending on the method of averaging. This increase has little influence on the conclusions in this paper; its basis is discussed in detail in Appendix A of Dame *et al.* (1985).

We estimate the amount of "background" mass excluded by clipping by assuming that background emission obeys the same CO to hydrogen scaling law as does cloud emission, and that background emission arises from the distance of the cloud nearest in angle and velocity. Then for an idealized model in which the clip threshold equals half the typical peak line intensity, the mass excluded by clipping is 0.7–2.0 times the mass included by clipping, for reasonable ranges of background intensity (0.8–1.6 K) and of cloud line width at the clip threshold (5–10 km s^{-1}). This result suggests that the background mass excluded by the present level of clipping may be comparable to, but does not greatly exceed, the deduced cloud mass in our sample, $\sim 10^8 \ M_\odot$.

c) H II Regions

The 68 H II regions selected as described in § III*a* have been placed on Figure 3 according to the (l, b)-coordinates of the peak emission and the $V_{\rm LSR}$ of the peak H 110α line intensity. The source-integrated flux density is coded by the size of the circle, as indicated in the inset. The correlation of H II regions with molecular clouds is remarkably good. Only five H II regions lie more than 0°.1 beyond the outer contour of a molecular cloud, and most of these five are at the far kinematic distance, where associated CO emission may have been missed owing to beam dilution. Therefore, location of an H II region within the CO emission contours of Figure 3 is probably a good criterion of association. This high rate of coincidence also suggests that the clip threshold, discussed in § IV*a*, has not been set unrealistically high.

d) Relative Positions of CO Cloud Peaks and H II Regions

The high density of molecular clouds and H II regions in the inner Galaxy makes it inevitable that unrelated clouds and H II regions will occasionally line up, and the near-far distance ambiguity allows such well-separated objects to have the same radial velocity. We have examined our data in two ways to test whether a significant number of the associations resulting from the criterion in § IV*c* are spurious in this sense, and we find this number to be insignificant. Here we show the first of these tests, a comparison of histograms of relative position between H II regions and peaks of CO emission; in § IV*e* we compare histograms of relative velocity.

By analogy with the Orion Nebula, M17, W3, and other nearby H II regions, a molecular cloud should have enhanced CO emission near an associated H II region. Such CO enhancement is visible at many locations in Figure 3. Therefore we made a histogram of the angular distance from the position of each H II region in our sample to the nearest local maximum of integrated antenna temperature in the CO map. This is shown in Figure 4 as "first quadrant" sources. To test this distribution for evidence of spurious associations, we constructed a "control group" of H II regions known to be associated with CO clouds. We used a sample of optically visible H II regions (20 from Israel 1978; 12 from Blitz, Fich, and Stark 1982) believed to be associated with CO emission on the basis of position agreement among their optical photographs, radio continuum maps, and CO emission maps, and velocity agreement between their CO and radio recombination lines. To these 32 regions we added three optically invisible H II regions (W3, W49, W51) whose detailed radio continuum and CO maps show strong evidence of interaction and thus of association. For this "standard" sample of 35, the CO and radio continuum maps were made with much finer angular resolution than were the maps in the first-quadrant sample. Nearly all the CO maps were made with the University of Texas Millimeter Wave Observatory, with FWHM beam 2'.3; and most of the radio continuum maps were made with the Westerbork Synthesis Radiotelescope, with FWHM synthesized beam $\sim 10''$.

We assume that the uncertainty in each source position θ_s due to effects of resolution, sampling, and gridding is proportional to the FWHM beam width, i.e., $\sigma_{\theta_s} = a\Delta\theta_b$, where a is a constant of order unity. Then the uncertainty in the relative

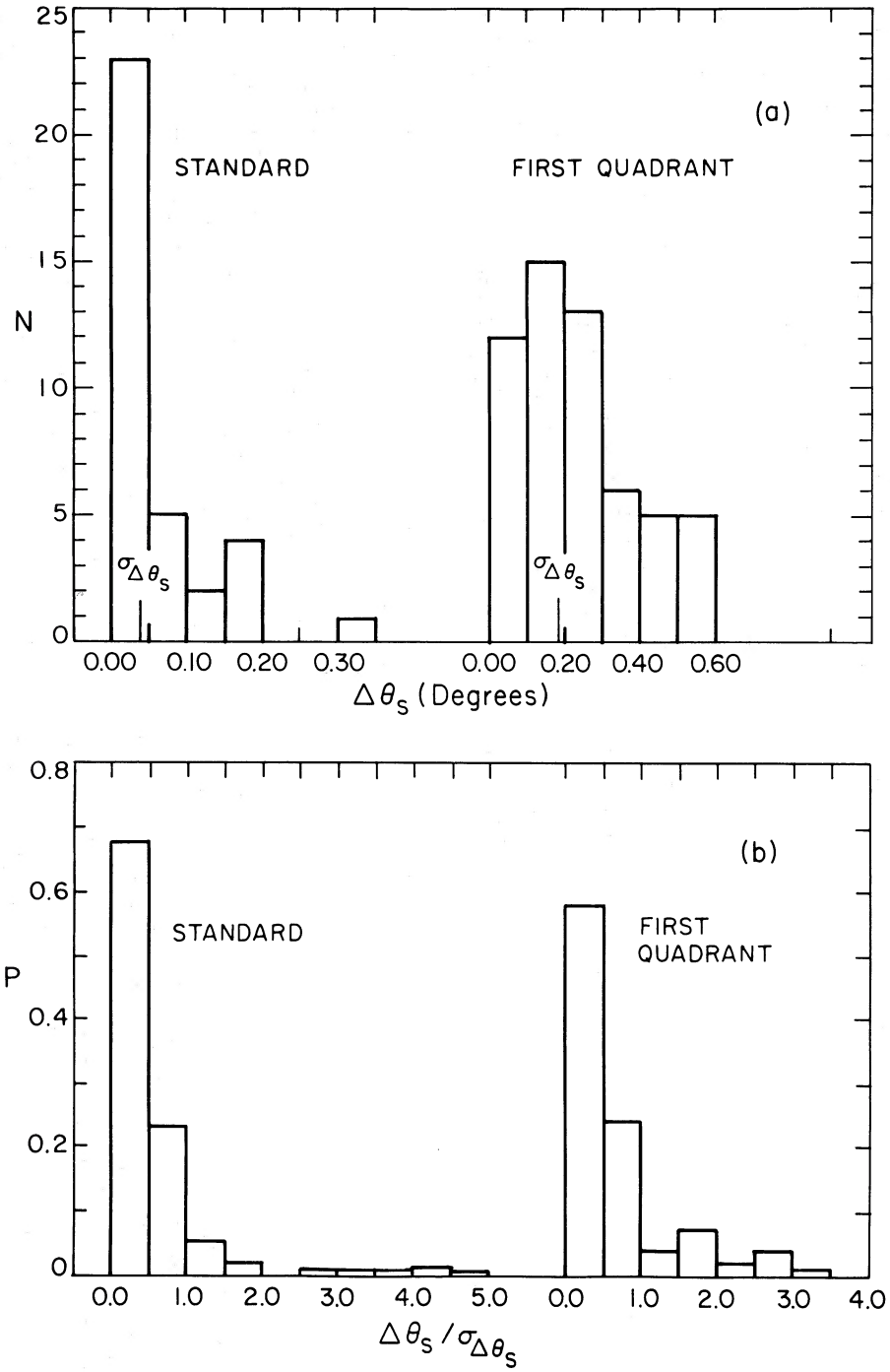

FIG. 4.—Distribution of angular offset $\Delta\theta_s$ between an H II region and the nearest peak of CO emision. (*a*) Comparison of histogram for a standard sample of relatively nearby H II regions known to be associated with molecular clouds with histogram for first-quadrant clouds studied in this paper. In each plot, the estimated uncertainty in $\Delta\theta_s$, $\sigma_{\Delta\theta_s}$ is marked by a labeled tick. (*b*) Distributions of relative probability of angular offset $\Delta\theta_s$, expressed in units of $\sigma_{\Delta\theta_s}$, obtained from distributions in (*a*) by dividing the number of sources in a bin by the angular area corresponding to that bin.

position $\Delta\theta_s = \theta_s(1) - \theta_s(2)$ is $\sigma_{\Delta\theta_s} = a[\Delta\theta_{b1}^2 + \Delta\theta_{b2}^2]^{1/2}$. For $a = 1$, the values of $\sigma_{\Delta\theta_s}$ are then 0°.038 for the standard sources and 0°.18 for the first-quadrant sources. In Figure 4*a* a vertical tick is shown at each of these values. Figure 4*a* suggests that the standard and first-quadrant histograms may be similar when the angular distance coordinate $\Delta\theta_s$ is expressed in terms of its uncertainty $\sigma_{\Delta\theta_s}$.

As a test we binned the standard and first-quadrant source data in units of $\sigma_{\Delta\theta_s}/2$, for $a = 1$, obtained the cumulative distributions, and applied the Kolmogorov-Smirnov two-sample two-tailed test (Siegel 1956, Table M). This test indicates that the distributions are statistically indistinguishable for all tabulated levels of significance (significance ≤ 0.10). Reasonable changes in binning or in the parameter a do not change this conclusion. Thus for each sample, the histogram of relative angular position between an H II region and the nearest CO peak is dominated by source pairs closer together than the uncertainty in relative position, and there is no significant evi-

dence for spurious associations in the first quadrant sources. To further illustrate this point, we show in Figure 4*b* the distributions of relative probability P of finding the nearest CO peak at angular distance $\Delta\theta_s$, where $\Delta\theta_s$ is expressed in units of $\sigma_{\Delta\theta_s}$. The similarity of the standard and first-quadrant distributions is then clearly visible.

e) Relative Velocities of CO *Clouds and* H II *Regions*

As a further check on the attribution of H II regions to molecular clouds, we compare the CO and recombination line velocities for the first-quadrant and standard cloud samples described in § IV*d*. For each H II region peak in the position-velocity map (§ III*a*), we obtained the difference in velocity $\Delta V \equiv V_{CO} - V_{H\,II}$ between the recombination line velocity at the position of strongest continuum emission and the velocity of the nearest peak in the spectrum of CO emission at the same position. The histogram of these first-quadrant velocity differences is shown in Figure 5, with that for the standard regions for comparison. The standard sample was selected in essentially the same way as in § IV*d*, but it has some different members because some regions lack CO maps, while others lack recombination line velocities. These histograms of relative velocity are not dominated by resolution effects as are the histograms of relative position in § IV*d*. The first-quadrant and standard histograms have about the same width, FWHM ≈ 9 km s^{-1}. The first-quadrant histogram is centered at 0 km s^{-1}, while the standard histogram is centered at ~ 3 km s^{-1}, as noted by Israel (1978). Since the standard sample was optically selected, the H II regions tend to lie in front of their molecular clouds. Therefore ΔV is generally positive as the H II region gas flows away from its cloud. The first-quadrant sample was not optically selected, so there is no reason to expect such a bias in the distribution of ΔV. Thus in comparison to the standard distribution of relative velocities, that for the first quadrant has no abnormality in width or center velocity and no unusually large wings that would suggest spurious association. Application of the Kolmogorov-Smirnov test as in § IV*d* indicates that the two distributions are again statistically indistinguishable, regardless of whether one shifts the standard sample by 3 km s^{-1}.

Based on these tests in §§ IV*d* and IV*e*, we conclude that location of an H II region within the outermost contour of CO emission from a cloud in Figure 3 gives no significant evidence for spurious associations. It is therefore an adequate criterion of association, and the H II region entries in Table 2 satisfy this criterion.

f) Distributions of H II *Regions and Molecular Clouds*

Figure 6 presents histograms of number of clouds versus log cloud mass for (*a*) clouds with associated H II regions and (*b*) clouds without associated H II regions. These histograms are not corrected for beam dilution of distant clouds. They show that in each group most of the mass is in the most massive clouds, as found by Dame *et al.* (1985), Sanders, Scoville, and Solomon (1985), and others. Consequently, the mean mass of clouds with H II regions, $2.6 \times 10^6\ M_\odot$, differs only slightly from the mean mass of clouds without H II regions, $1.1 \times 10^6\ M_\odot$. However the histograms differ significantly at the low-mass end: six of the 22 clouds with no H II regions have mass less than $10^5\ M_\odot$, while only one of the 32 clouds with H II regions has mass less than $10^5\ M_\odot$. Furthermore, the association of the H II region with this one cloud (38,16) is uncertain; see the discussion in Appendix A. The Kolmogorov-Smirnov test described earlier indicates that the two samples are probably distinct: the likelihood that they would arise from the same parent distribution is about 0.05. The present results are consistent with the finding that massive stars tend to be absent from low-mass clouds (Myers 1977) and allow the quantitative conclusion that H II region radio continuum emission stronger than 1 Jy is found primarily in clouds more massive than $10^5\ M_\odot$. If, as discussed in §§ IV*b* and VII*a*, one instead considers a

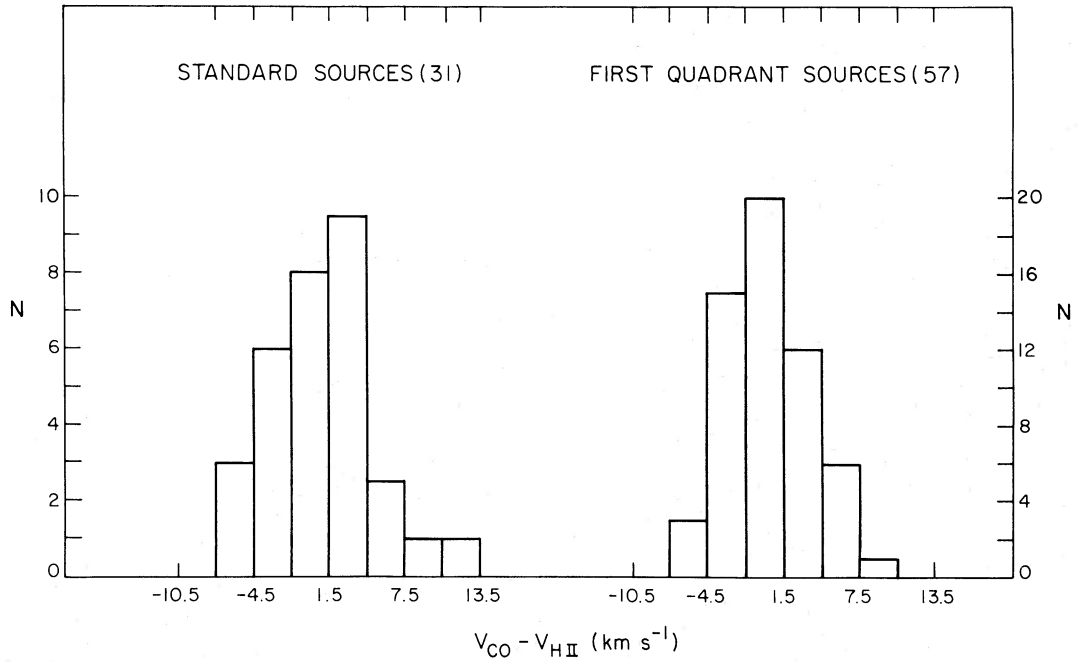

FIG. 5.—Distributions of relative LSR velocity $V_{CO} - V_{H\,II}$, where $V_{H\,II}$ is the recombination line velocity of an H II region and V_{CO} is the velocity of peak CO emission at the position of the H II region, for standard and first-quadrant sources as described in the legend to Fig. 4 and in the text.

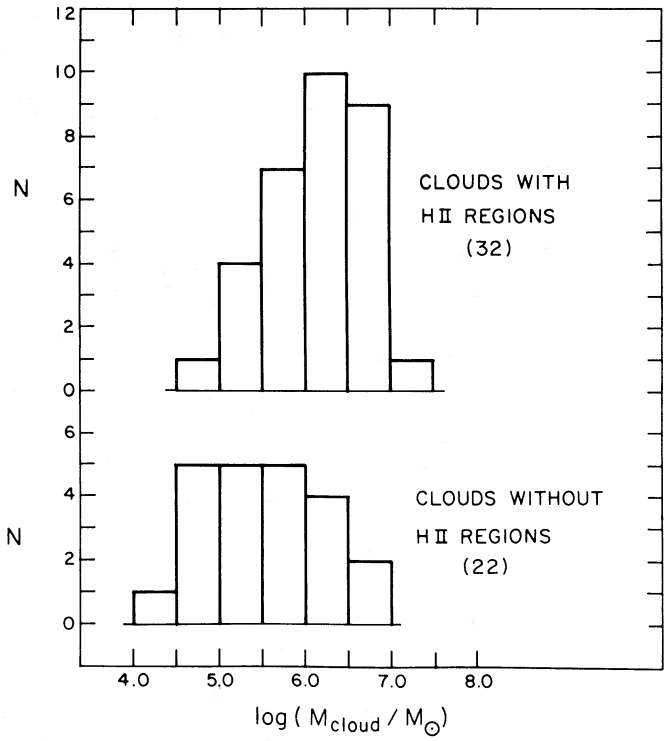

FIG. 6.—Distributions of log cloud mass, for first-quadrant clouds (*top*) with associated H II regions and (*bottom*) without H II regions

"cloud" to be a single local maximum in Figure 3, then the numbers change, but the conclusion does not: 27 of the 84 clouds without H II regions have mass less than $10^5\ M_\odot$, while only two of the 65 clouds with H II regions have mass less than $10^5\ M_\odot$.

The distribution of clouds in the Galactic plane is shown in Figure 7. The format is similar to that of Figure 6 of Dame *et al.* (1985): each cloud is represented by a circle whose diameter is proportional to the cube root of the cloud mass. The circles are shaded to indicate the FIR luminosity (§§ V and VI) due to sources associated with each cloud. The FIR luminosity is a good approximation to the total luminosity, as discussed in § VI*a*. When a FIR source was too weak or too confused to give a reliable estimate of FIR luminosity, the measurement of, or limit on, the radio continuum flux density was used to indirectly estimate the FIR luminosity (§ V*b*).

The distribution of clouds in Figure 7 does not differ significantly from that of Dame *et al.*; the 21 clouds that are not in the sample of Dame *et al.* mainly add detail at small and large distance from the Sun. The Sagittarius arm appears relatively well defined. It extends along an arc from a point with $l = 15°$ and radial distance from the Sun $r = 1$ kpc to $(l, r) = (25°,$ 14 kpc). The preponderance of low-mass clouds without H II regions, discussed above, is also evident here: such clouds are primarily local, and beyond about 10 kpc would fall below the survey sensitivity limit. There are three very massive clouds ($M > 10^{6.5}\ M_\odot$) that have weak FIR luminosity: 29,80; 37,82; and 31,48. The most luminous sources lie within ~6 kpc of the Galactic center. However, it appears that the more massive molecular clouds delineate the Sagittarius arm more clearly than do the more luminous H II regions. This may occur because from cloud to cloud along the arm, the relative variation of cloud mass is much smaller (a factor of ~15) than the relative variation of luminosity (a factor of ~500).

V. H II REGION/FIR SOURCE LUMINOSITIES

a) FIR Source Luminosity

FIR emission from first-quadrant sources associated with H II regions is superposed on a bright extended background, and it is necessary to properly separate the background contribution to deduce source properties. Observations at several FIR wavelengths (Hauser *et al.* 1984) indicate that emission from both source and background regions is optically thin. In this case, a simple model indicates that subtraction of a background intensity from the observed intensity is significantly more accurate that clipping (see Appendix B). Therefore we use subtraction rather than clipping for background removal from all FIR sources.

We obtained and subtracted a local estimate of the background at 24 of the 36 positions of peak 150 μm emission in the source list of Hauser *et al.* (1984, Table 3) that lie within 0°.3 of the peak of an H II region and then computed color temperature and FIR luminosity for each of these 24 sources. The details of this procedure are given in Appendix C.

The FIR luminosities, given in column (12) of Table 2, range from $\sim 10^5$ to $\sim 10^8\ L_\odot$ for W49. Each luminosity has an estimated random uncertainty of a factor of a few, due to uncertainties in background level and source distance. If the FIR emissivity varies with wavelength λ as λ^{-1} rather than as λ^{-2}, as assumed here, the typical luminosity will increase by a factor of ~2. FIR observations with 0°.4 resolution by Boissé *et al.* (1981) of the prominent sources M17, W43, W44, W49, and W51 have luminosities greater than those deduced here by a mean factor of 2.0, owing probably to the larger area attributed by Boissé *et al.* to each source. FIR observations with 1′ resolution of G12.8 − 0.2 and M17 (Jaffe, Stier, and Fazio 1982) and M16 (McBreen, Fazio, and Jaffe 1982) yield luminosities less than those reported here by a mean factor of 1.6. Consider-

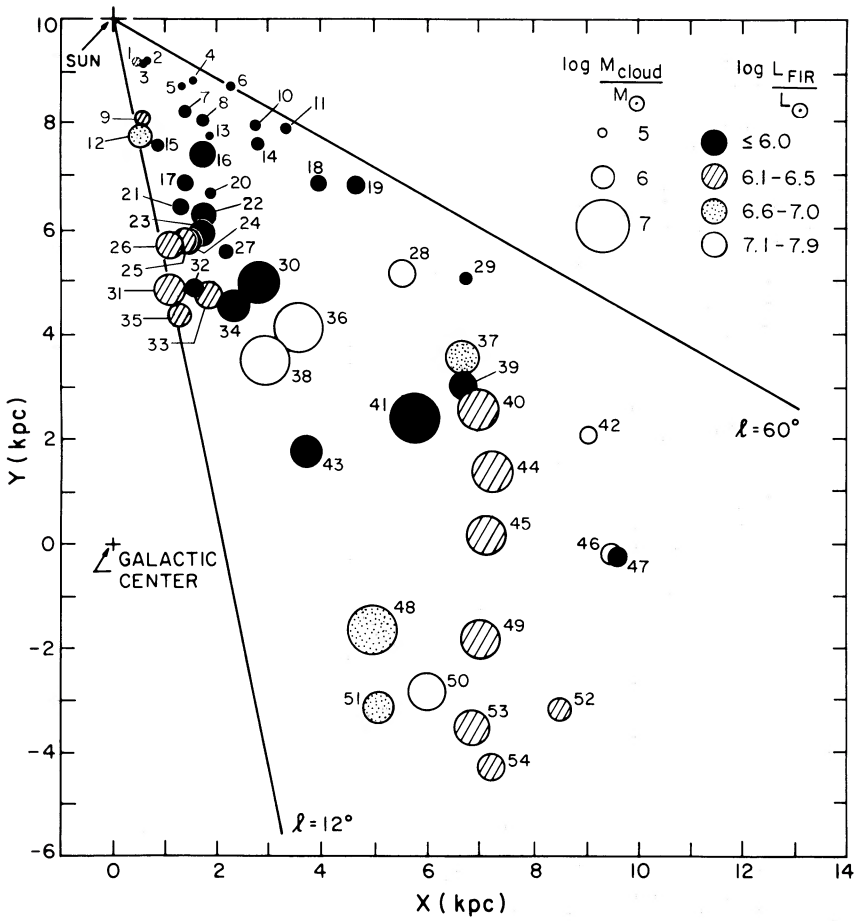

FIG. 7.—Positions of first-quadrant clouds in the Galactic plane. The diameter of each circle is proportional to the cube root of M_{cloud}, and the shading represents the FIR luminosity due to sources in the cloud, as indicated in the inset. Clouds are identified according to the following scheme:

Label	Name	Label	Name	Label	Name	Label	Name	Label	Name	Label	Name
1.....	31,12	10.....	53,60	19.....	56,36	28.....	49,59	37.....	46,59	46.....	43,11
2.....	38,16	11.....	58,37	20.....	29,52	29.....	54,40	38.....	24,98	47.....	42,16
3.....	35,13	12.....	14,20	21.....	20,42	30.....	29,80	39.....	44,60	48.....	23,78F
4.....	53,24	13.....	39,42	22.....	25,55N	31.....	12,45	40.....	43,63	49.....	31,48
5.....	46,25	14.....	50,45	23.....	22,53	32.....	17,58	41.....	37,82	50.....	25,55F
6.....	60,27	15.....	20,25	24.....	18,48	33.....	19,65	42.....	49,18	51.....	21,60
7.....	39,32	16.....	35,44	25.....	17,44	34.....	23,78N	43.....	24,110	52.....	33,10
8.....	41,37	17.....	24,42	26.....	14,39	35.....	13,54	44.....	40,59	53.....	27,34
9.....	17,22	18.....	51,55	27.....	26,65	36.....	31,95	45.....	36,57	54.....	27,25

ing the many uncertainties involved, these comparisons indicate reasonably good agreement among the FIR observations.

b) Lyman-Alpha Luminosity

To estimate the number and spectral type of the stars associated with each molecular cloud, we first calculate $L_{Ly\alpha}$, the luminosity in the Lyman-α line that would be emitted by an H II region if each stellar Lyman-continuum photon absorbed by the gas were degraded through recombination to a Lyα photon. We use $L_{Ly\alpha} = N'_c h\nu_{Ly\alpha}$, where N'_c is the number of Lyman-continuum photons absorbed by the gas and is deduced from the observed radio continuum emission (Mezger, Smith, and Churchwell 1974). Then

$$L_{Ly\alpha} = 2.36 \times 10^4 T_e^{-0.45} S_\nu(5\ \mathrm{GHz}) D^2\ L_\odot\ , \qquad (2)$$

where T_e (in K) is the electron temperature from Downes *et al.* (1980); S_ν(5 GHz) (in Jy) is the flux density integrated over each source in the synthetic H II region map (§ III*a*), and D (in kpc) is the adopted distance to the associated molecular cloud. When a molecular cloud lacks H II regions, we calculate the upper limit on $L_{Ly\alpha}$ for a single H II region on the assumption that $S_\nu(5\ \mathrm{GHz}) < 1$ Jy—the limit employed by Downes *et al.* (1980)—and that $T_e = 7000$ K. The values of log $L_{Ly\alpha}$ are given in column (9) of Table 2.

VI. STELLAR MASSES AND STAR FORMATION EFFICIENCIES

a) Masses from Lyα *and FIR Luminosities*

We now combine the Lyα and FIR luminosities derived in §§ V*a* and V*b* to investigate the behavior of the infrared excess and to make estimates of the total mass of stars needed to account for the observed luminosities.

The infrared excess (IRE), defined by Mezger (1978) as IRE $\equiv L_{\rm FIR}/L_{\rm Ly\alpha}$, is a measure of the heating of dust associated with H II regions. If IRE = 1, the FIR luminosity can be explained by stellar Lyα photons, which, after absorption by the gas and degradation to Lyα, are absorbed by dust grains. If IRE > 1, either direct dust absorption of stellar photons or additional stars producing little ionization, or both, are needed. Most observations of Galactic H II regions give IRE > 1, as do those considered here. For the 25 sources with values of both $L_{\rm FIR}$ and $L_{\rm Ly\alpha}$ in Table 2, Figure 8 shows log $L_{\rm FIR}$ versus log $L_{\rm Ly\alpha}$, with straight lines indicating IRE = 1, 10, and 100 (the curved line marked "single-cluster model" will be discussed in § VI*b*). These data show that $L_{\rm FIR}$ and $L_{\rm Ly\alpha}$ are correlated; this correlation supports our claim that the choices of associated sources are generally correct. The median IRE for these sources is 6—a value similar to the mean IRE of 9 reported by Hauser *et al.* (1984), based on the same data, but with no background subtracted; and similar to the IREs of the more luminous sources observed with high resolution in the M17–W33 region by Jaffe, Stier, and Fazio (1982). However, these values are 3–10 times lower than some of those found by Gispert, Puget, and Serra (1982, hereafter GPS) from FIR data with a coarser angular resolution of 0°.4.

GPS also found a significant decrease in IRE with increasing galactocentric radius, but there is no evidence in our data for such a trend. In Figure 9, we plot the data in Figure 8 and those of GPS as log IRE versus galactocentric radius R. Where the GPS data and our data correspond to the same source, with no ambiguity due to differing resolutions, the two data points are joined by a straight line. The IRE values of GPS are generally higher than ours, due largely to the relatively high FIR flux they attribute to each source. This in turn may be due to the larger area of each GPS source. Thus GPS sources include FIR emission that we consider background, and the proportion of such emission is greater in the FIR than in the radio continuum. Also, the larger beam of GPS may include luminosity contributions from low-mass stars distributed widely throughout molecular clouds, while the narrower beam of Hauser *et al.* may sense a higher proportion of emission from massive stars. Since these effects depend strongly on angular resolution, one expects them to be most pronounced for the most distant sources considered here, i.e., sources with smallest R. If so, the decline of IRE with R claimed by GPS, and the consequence that the inner Galaxy is relatively deficient in producing OB stars, may be artificial. A similar conclusion was reached by Odenwald and Fazio (1984).

To interpret the luminosities $L_{\rm Ly\alpha}$ and $L_{\rm FIR}$ derived from observations in terms of the stellar content of an H II region or complex of regions, we use the well-known method based on models and calculations of Petrosian, Silk, and Field (1972); Panagia (1973, 1974); and Mezger, Smith, and Churchwell (1974). Basically, the IRE of a complex measures P, the fraction

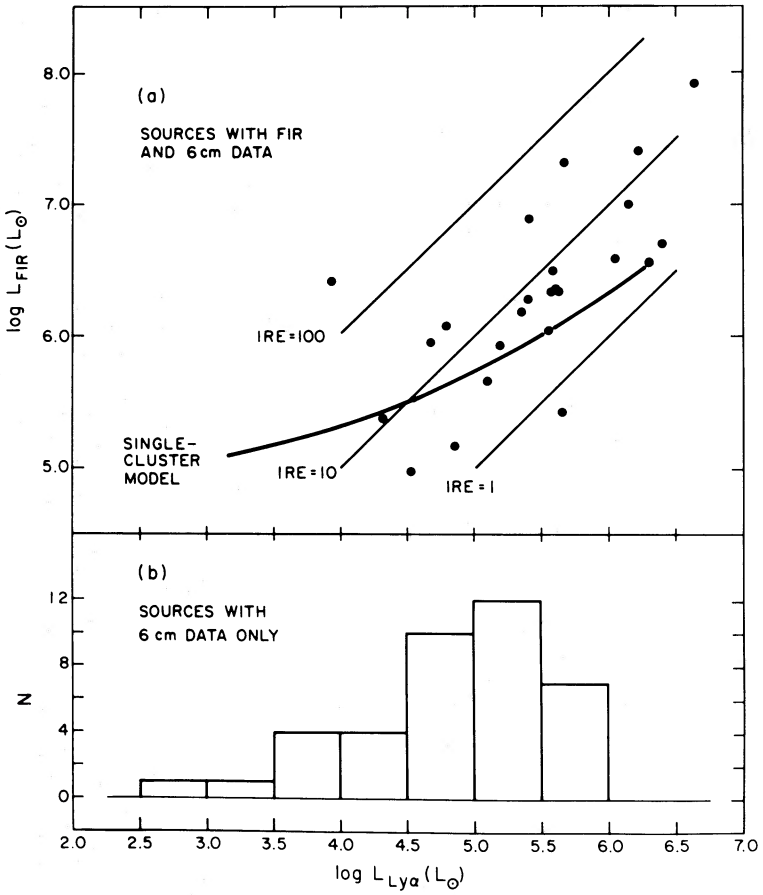

FIG. 8.—FIR and Lyα luminosities. (*a*) log $L_{\rm FIR}$ vs. log $L_{\rm Ly\alpha}$ for sources where both luminosities are available. Lines of constant slope indicate IRE values of 1, 10, and 100. The curved line gives the prediction of a model stellar cluster, whose mass distribution follows the initial mass function of Miller and Scalo (1979). (*b*) Distribution of log $L_{\rm Ly\alpha}$ for those sources where $L_{\rm FIR}$ is not available, showing that most of these sources have values of $L_{\rm Ly\alpha}$ for which the single-cluster model gives predictions of $L_{\rm FIR}$ in reasonable agreement with the available data.

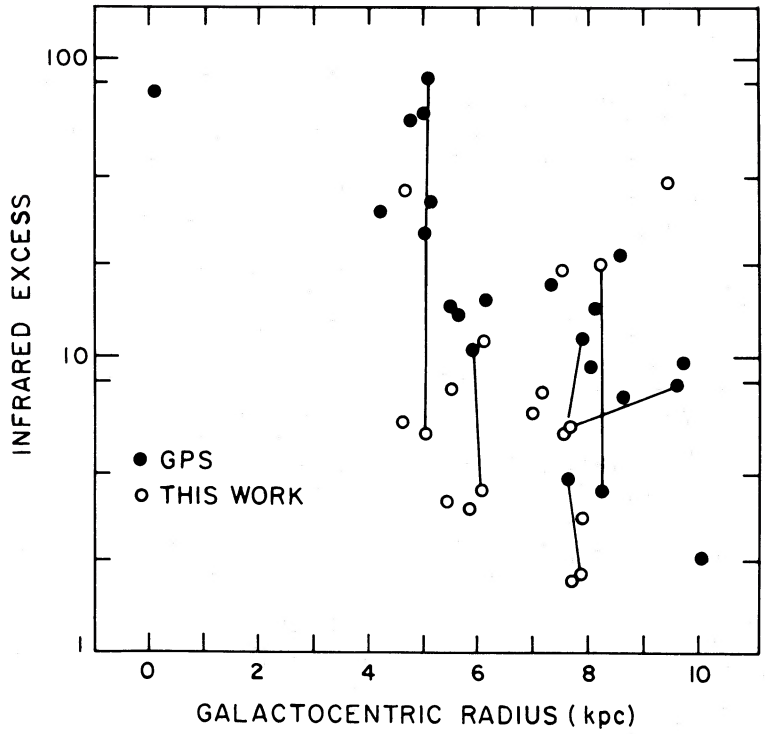

FIG. 9.—Infrared excess vs. galactocentric radius for sources with $L_{FIR} > 10^6\ L_\odot$, according to Gispert, Puget, and Serra (1982, *filled circles*) and this paper (*open circles*). Where the GPS data and our data correspond to the same source, with no ambiguity due to differing resolutions, the two points are joined by a straight line.

of stellar luminosity at frequencies above the Lyman limit. Therefore, the IRE is used to estimate the spectral type, or types, of the stars in the complex. Similarly, L_{FIR} is related to the total stellar luminosity L_*; thus it is used to estimate the total number of stars in the complex.

The fraction P of L_* in the Lyman continuum depends on the spectral type of each exciting star and is related to the IRE deduced from observations by

$$P = \frac{\theta}{(\mathrm{IRE})(x)} . \tag{3}$$

Here x is the fraction of Lyman continuum flux transformed into Lyα radiation, depending on spectral type and electron density n_e in the H II region (Panagia 1973). The quantity θ depends on spectral type, H II region dust optical depth τ_1, and circumnebular optical depth τ_5 (Panagia 1974). We consider as plausible the range of spectral types O9.5–O4, and the values $10^3 \leq n_e \leq 10^5$ cm^{-3}, $0.0 \leq \tau_1 \leq 0.5$, and $1 \leq \tau_5 \leq \infty$. Over these ranges, $1.1 \leq \theta/x \leq 4.8$. However, the parameters within these ranges do not change independently, and the following cases are probably more realistic: (1) A hot star in a young, dense, compact H II region with very little dust in the H II region and high circumnebular extinction—a combination suggested by Tielens and de Jong (1979) for W3 A/IRS 1. We assume an O6 star, electron density 10^5 cm^{-3}, $\tau_1 = 0$, and $\tau_5 = \infty$, giving $\theta/x = 2.3$. (2) In contrast, a cooler star in a more evolved, rarefied, and extended H II region is likely to have more internal and less external dust. For an O9.5 star with $n_e = 10^3$ cm^3, $\tau_1 = 0.5$, and $\tau_5 = 1.0$, $\theta/x = 2.7$. Consequently, we adopt $\theta/x = 2.5$, with uncertainty of a factor of 2; then

$$P = \frac{2.5}{\mathrm{IRE}} . \tag{4}$$

To obtain the total stellar luminosity L_*, we assume that essentially all of L_* emerges as observed FIR luminosity, i.e., $L_* = L_{FIR}$. According to Panagia (1974), an H II region ionized by an O6 star will have $L_{FIR}/L_* \geq 0.8$, provided the visual circumnebular absorption (τ_5) is greater than 0.8 mag. This condition is easily satisfied by the FIR sources considered in this paper, since they are all associated with molecular clouds. Even if some are "blisters" (Israel 1978), each blister will have significant dust optical depth on its molecular cloud side. According to equation (1), the column density corresponding to the weakest emission recorded in the Cohen *et al.* (1980) CO survey ($\int T_{12}\, dv \approx 10$ K km s^{-1}) is $N \approx 2 \times 10^{21}\ H_2$ molecules cm^{-2}, or $A_V \approx 2$ mag. Thus, $\tau_5 > 0.8$ mag, and the adopted relation $L_* = L_{FIR}$ is probably accurate within 20%.

We now compare P and L_* deduced from observation of an H II region complex to those predicted for $N_{cluster}$ identical clusters of stars, each of which follows the initial mass function (IMF) of Miller and Scalo (1979):

$$\xi(\log m) \propto \exp\,[-1.09(\log m + 1.02)^2] . \tag{5}$$

The minimum stellar mass in the IMF is assumed to be 0.1 $M_\odot$. Ho and Haschick (1981) present luminosity calculations for this distribution, normalized to one star of the maximum mass m_{max} in the interval $\Delta \log m_{max} = 0.04$ around $\log m_{max}$. We use these calculations and the observed IRE to obtain m_{max}. Then $N_{cluster}$ is obtained from the ratio of the observed L_* to the predicted total luminosity of a cluster with the deduced value of m_{max}. The total stellar mass, hereafter denoted m, is then $N_{cluster}$ times the mass of one cluster having the deduced m_{max}. This cluster mass was computed by integrating over the IMF from 0.1 $M_\odot$ to m_{max}. The calculated values of m_{max}, $N_{cluster}$, and m are given in Table 3.

This method may sometimes underestimate the stellar content because it assumes that (1) the IMF of field stars

TABLE 3

STELLAR MASS ESTIMATES BASED ON 6 cm, 150 μm, AND 250 μm MEASUREMENTS

FIR Source	log L(FIR) ($L_\odot$)	IRE	log m_{max} ($M_\odot$)	$N_{cluster}$	log m ($M_\odot$)
12.9 − 0.2.....	6.3	5.2	...	...	...
14.5 + 0.0.....	6.5	7.9	1.8	0.3	4.3
15.0 − 0.7.....	6.6	1.8	...	...	...
16.3 − 0.2.....	6.4	300	1.2	22	4.9
17.1 + 0.8.....	6.1	20	1.5	1.0	4.2
18.2 − 0.3.....	5.7	3.5	...	...	...
19.0 − 0.1.....	5.4	11	1.7	0.06	3.4
20.6 − 0.3.....	6.6	3.0	...	...	...
23.3 − 0.2.....	6.9	35	1.4	13	5.1
24.4 + 0.1.....	5.4	0.7	...	...	...
24.8 + 0.1.....	5.9	5.7	...	...	...
25.4 − 0.2.....	7.4	17	1.6	16	5.4
26.2 + 0.0.....	6.4	5.6	...	...	...
29.8 − 0.1.....	6.0	3.1	...	...	...
30.6 − 0.2.....	7.0	7.0	1.8	0.6	4.7
34.2 + 0.2.....	6.0	17	1.6	0.6	4.1
35.5 + 0.1.....	5.0	2.6	...	...	...
37.7 − 0.3.....	6.3	6.1	...	...	...
41.0 − 0.2.....	6.2	6.8	1.8	0.1	4.0
43.2 + 0.0.....	7.9	19	1.5	68	6.0
45.5 + 0.1.....	6.3	5.0	...	...	...
48.8 + 0.1.....	7.3	39	1.4	39	5.5
49.6 − 0.3.....	6.4	1.8	...	...	...
54.1 + 0.0.....	5.2	2.1	...	...	...
Median	6.3	5.7	...	...	4.7

NOTE.—Blank in the last three columns indicates that the IRE is too low to be consistent with the IMF cluster model.

applies to molecular clouds, and (2) the number $N_{O,\,now}$ of O stars now in a molecular cloud is essentially all the $N_{O,\,all}$ O stars that the cloud has produced during its lifetime. If significant O star production occurred in the past, then m must be increased by a factor $R = N_{O,\,all}/N_{O,\,now}$, with $R \geq 1$. We have no way to reliably estimate R for each cloud, and the significant variation in stellar mass that we will find from cloud to cloud may be greater than that of R. Therefore we assume $R = 1$ for the following calculations of stellar mass in individual clouds—not a serious restriction, since the main purpose here is to identify those clouds with extremely low and extremely high stellar mass. In Sections VII*c–e* we consider the likely range of R and implications of $R > 1$.

On the other hand, this method may sometimes overestimate the stellar content because: (1) Stars in clouds could obey the IMF in an average over many clouds but could have large departures in individual clouds, as suggested by the work of Güsten and Mezger (1982) and Solomon, Sanders, and Rivolo (1985): some clouds could have mainly low-mass stars, and others (such as those considered here), mainly massive stars. The IMF cluster estimate would thus attribute more low-mass stars to these latter clouds than are actually present. (2) Recent, extensive observations of early-type O stars (Garmany, Conti, and Chiosi 1982; Bisiacchi, Firmani, and Sarmiento 1983) imply a higher proportion of massive stars than Miller and Scalo obtained. Comparison of the mass in a cluster that follows the Miller-Scalo IMF, calculated as described above, with the mass in a cluster that follows case (*b*) of Garmany, Conti, and Chiosi for log $m \gtrsim 1.2$ indicates that the Miller-Scalo mass is greater by a factor of 2–4 if the most massive cluster star has spectral type O7–O4.

In about half the cases in Table 3, m cannot be calculated because the IRE is too low (IRE < 6.8) to be consistent with a Miller-Scalo cluster. Undoubtedly, some of the inconsistent cases arise from inaccuracy in the IRE. There are several ways in which some of this inconsistency could be resolved by changes in our analysis: (1) the high-mass end of the IMF could be modeled by that of Garmany, Conti, and Chiosi (1982) as described above; (2) a higher low-mass cutoff to the IMF than 0.1 $M_\odot$ could be used; (3) a FIR emissivity exponent less negative than −2.0, e.g., −1.5, could be used. However, the impact of these changes on the range of stellar mass estimates in this paper is fairly small. We take the high rate of inconsistency to mean that the estimates of m for individual H II region/FIR complexes are highly uncertain, by perhaps factors of 5–10, and that such estimates are best used in averages over many clouds.

In some cases in Table 3, a more subtle inconsistency appears between the values of L_* and the IRE, and the IMF cluster model. When $N_{cluster}$ is significantly less than unity, the most massive members of the hypothetical cluster contribute less than one stellar mass to the cluster mass—an unphysical situation. When $N_{cluster}$ is significantly more than unity, the distribution of stellar mass departs from the IMF at the high-mass end because the bin of the most massive cluster member is filled $N_{cluster}$ times, while the next higher mass bin is empty—thus the slope of the adopted distribution is much steeper than that of the true IMF at $m = m_{max}$. To see whether either of these inconsistencies leads to an unacceptable estimate of the total mass m, we compared predictions of m when $N_{cluster} = 0.1$ and 10 to analogous predictions of a model where $N_{cluster}$ is forced to be unity and where L_*, not the IRE, determines m_{max}. In each case, the single-cluster model agrees with the present model to within 20%. Therefore we consider the present model acceptable even when $N_{cluster}$ departs significantly from unity.

b) Masses from Lyα Luminosity Alone

As discussed above, the FIR flux associated with an H II region is not always known reliably in both FIR channels; and for some H II regions with reliable FIR fluxes, the deduced luminosities $L_{Ly\alpha}$ and L_{FIR} are inconsistent with the models of IMF clusters. In each of these cases, the procedure just described to estimate m cannot be used. As an alternate estimate of m, we use the Lyα luminosity and the same model of an IMF cluster as in § VI*a* but with $N_{cluster}$ assumed to be unity. This model predicts a specific value of L_{FIR} for each $L_{Ly\alpha}$, and this value of L_{FIR} agrees reasonably well with the available data, as Figure 9 shows. These results are summarized in Table 4. The median cluster mass is then $1 \times 10^4\ M_\odot$, ~5 times less than in Table 3.

c) Relative Variation of Star and Cloud Masses

The values of M_*, the total stellar mass in a cloud, are plotted in Figure 10 as a function of the cloud mass M_{cloud} in order to investigate the relationship between star and cloud mass. Here M_* is the sum of m in Table 4 for each H II region associated with the cloud. The figure shows a trend in which $M_* \propto M_{cloud}^p$, where $p \approx 0.5$. The apparent correlation between log M_{cloud} and log M_* is unlikely to be due to chance: both the best-fit line through all the data points, marked "1" in Figure 10, and the best fit through all but the two highest points, marked "2," have probability below 0.01 of arising by chance. The equation of fit 1 is log $M_* = 2.1 + 0.38$ log M_{cloud}, with 1 σ uncertainties in intercept and slope of 1.0 and 0.17 respectively. The equation of fit 2 is log $M_* = 1.3 + 0.50$

TABLE 4

STELLAR MASS ESTIMATES BASED ON 6 cm MEASUREMENTS ALONE

H II Region	log L(Lyα) ($L_\odot$)	log m ($M_\odot$)
12.8 − 0.3.....	5.62	4.2
13.1 + 0.0.....	4.85	3.9
13.9 + 0.3.....	4.52	3.8
14.0 − 0.1.....	4.44	3.8
14.5 − 0.6.....	3.69	3.7
15.1 − 0.6.....	6.30	4.5
17.0 + 0.9.....	4.78	3.9
18.3 − 0.3.....	5.11	4.0
18.9 − 0.5.....	5.61	4.2
19.1 − 0.3.....	4.95	3.9
19.5 + 0.1.....	5.14	4.0
19.6 − 0.3.....	4.70	3.9
20.1 − 0.1.....	3.86	3.7
20.8 − 0.1.....	6.06	4.4
21.0 + 0.1.....	3.49	3.6
22.8 − 0.5.....	5.32	4.1
23.0 − 0.4.....	5.71	4.2
23.9 − 0.1.....	4.93	3.9
24.0 + 0.1.....	5.28	4.1
24.5 − 0.3.....	5.56	4.1
24.5 + 0.3.....	5.66	4.2
24.5 + 0.5.....	5.65	4.2
24.8 + 0.1.....	5.18	4.0
25.3 + 0.3.....	3.65	3.7
25.8 + 0.3.....	5.87	4.3
26.1 − 0.1.....	5.61	4.2
26.5 + 0.4.....	5.23	4.0
27.3 + 0.1.....	5.07	4.0
27.5 + 0.1.....	5.47	4.1
28.6 + 0.0.....	5.39	4.1
30.0 + 0.0.....	5.56	4.2
30.3 − 0.1.....	4.68	3.9
31.1 + 0.0.....	4.71	3.9
31.4 − 0.3.....	4.44	3.8
31.4 + 0.3.....	4.47	3.8
32.8 + 0.3.....	5.54	4.1
33.9 + 0.1.....	4.42	3.8
35.0 − 0.5.....	3.83	3.7
35.6 + 0.0.....	4.53	3.8
37.4 + 0.0.....	5.59	4.2
37.9 − 0.4.....	5.39	4.1
39.3 + 0.0.....	2.95	3.5
41.5 + 0.0.....	5.15	4.0
42.1 − 0.6.....	5.04	4.0
43.1 − 0.5.....	4.65	3.9
45.1 + 0.1.....	5.32	4.1
45.5 + 0.1.....	5.57	4.2
46.5 − 0.3.....	5.28	4.1
48.9 − 0.3.....	5.44	4.1
49.2 − 0.3.....	5.68	4.2
49.5 − 0.4.....	6.41	4.5
50.1 − 0.6.....	4.69	3.9
51.4 + 0.0.....	4.56	3.8
54.1 − 0.1.....	4.85	3.9
Median	5.15	4.0

log M_{cloud}, with uncertainties 0.71 and 0.12. We adopt 0.5 ± 0.2 as an estimate of the slope.

To test whether the apparent correlation between log M_* and log M_{cloud} reflects differing dependence of M_* and M_{cloud} on distance D, we plot the data in Figure 10 with three symbols, each representing a range of a factor of ~ 2 in D. These show that the slope evident in the entire sample is still present, although with reduced statistical significance, in each range of D, while the intercept decreases slightly with D. This change in intercept with D is small compared to the range in

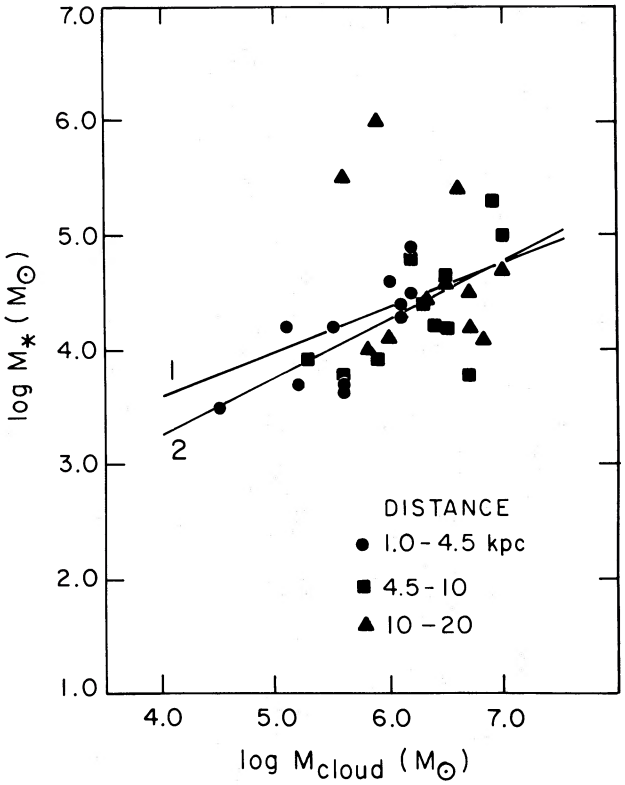

FIG. 10.—The total stellar mass M_* associated with a cloud vs. the mass M_{cloud} of the cloud, for a model in which the FIR and 6 cm emission are due to identical IMF clusters. The distance of each cloud from the Sun is coded as in the inset. Straight lines indicate least-squares fits of log M_* vs. log M_{cloud}, for (1) all points, and (2) all but the two highest points.

log M_* and is therefore relatively unimportant. These ranges of D are smaller than or similar to the ranges of the other observational variables that enter the calculation of M_* (5 GHz flux) and M_{cloud} (integrated CO intensity). Therefore the slope 0.5 ± 0.2 in Figure 10 is probably due neither to chance nor to distance effects but instead has a real basis. It is possible, however, that the true dependence of M_* on the factor R (assumed here to be unity) could substantially alter the correlation. Also, the correlation in Figure 10 would have reduced significance if, as discussed in § IVa, each local maximum in Figure 3 were considered a "cloud." Then the range of M_* decreases slightly while the range of M_{cloud} decreases by a factor of ~ 10 and scatter dominates the graph.

An increase in log M_* with increasing log M_{cloud}, as in Figure 10, is at least qualitatively consistent with several possible relations. If stars of all types form at largely random places and times in molecular clouds, massive clouds should contain more stars than less massive clouds simply because massive clouds present more opportunities for star formation. Alternatively, the stellar population and the cloud mass could both increase with time, for unrelated reasons. If so, older clouds would tend to have both more cloud mass and more stars than younger clouds. These and other possibilities are discussed by Larson (1982).

Larson also investigated the relationship between the mass m_{max} of the most massive star in a cloud and the cloud mass M_{cloud} for 27 clouds generally not covered by the surveys discussed in this paper. He found $m_{max} \propto M_{cloud}^{0.4}$ for $1.3 \lesssim \log (M_{cloud}/M_\odot) \lesssim 5.5$. The clouds considered here are more

TABLE 5

CLOUDS AND THEIR ASSOCIATED STARS: ESTIMATES OF MASS AND STAR FORMATION EFFICIENCY

Cloud	log M_{cloud} ($M_\odot$)	log M_* ($M_\odot$)	log SFE
12,45	6.5	4.2	−2.3
13,54	5.9	3.9	−2.0
14,20	6.0	4.6	−1.4
14,39	6.2	4.5	−1.7
17,22	5.5	4.2	−1.3
17,44	6.2	4.9	−1.3
17,58	5.8	<3.8	<−2.0
18,48	6.1	4.3	−1.8
19,65	6.3	4.4	−1.9
20,25	5.1	4.2	−0.9
20,42	5.6	3.7	−1.9
21,60	6.3	4.4	−1.9
22,53	6.2	<3.7	<−2.5
23,78N	6.4	<3.8	<−2.6
23,78F	7.0	4.7	−2.3
24,42	5.6	3.7	−2.9
24,98	6.9	5.3	−1.6
24,110	6.4	4.2	−2.2
25,55N	6.0	<3.7	<−2.3
25,55F	6.6	5.4	−1.2
26,65	5.5	<3.7	<−1.8
27,25	6.2	<4.0	<−2.2
27,34	6.5	4.6	−1.9
29,52	5.4	<3.7	<−1.7
29,80	6.7	3.8	−2.9
31,12	3.2	<4.0	<−0.06
31,48	6.6	<3.9	<−2.7
31,95	7.0	5.0	−2.0
33,10	6.0	4.1	−1.9
35,13	4.6	<3.4	<−1.2
35,44	6.1	4.4	−1.7
36,57	6.7	4.2	−2.5
37,82	7.0	<3.8	<−3.2
38,16	4.5	3.5	−1.0
39,32	5.0	<3.6	<−1.4
39,42	4.7	<3.7	<−1.0
40,59	6.8	4.1	−2.7
41,37	5.1	<3.6	<−1.5
42,16	5.8	4.0	−1.8
43,11	5.9	6.0	−0.3
43,63	6.7	4.5	−2.2
44,60	6.2	<3.9	<−2.3
46,25	4.2	<3.6	<−0.7
46,59	6.5	4.6	−1.9
49,18	5.6	5.5	−0.4
49,59	6.2	4.8	−1.4
50,45	5.4	<3.7	<−1.7
51,55	5.6	3.8	−1.8
53,24	4.6	<3.6	<−1.0
53,60	5.0	<3.7	<−1.3
54,40	5.3	3.9	−1.4
56,36	5.7	<3.8	<−1.9
58,37	5.2	<3.7	<−1.5
60,27	4.9	<3.6	<−1.1
Median	5.8	4.3	−1.8

massive, having $5.0 \lesssim \log (M_{cloud}/M_\odot) \lesssim 7.0$. We have evaluated m_{max} for each of the 34 clouds in Table 5 having 6 cm flux density 1 Jy or more according to the IMF cluster method described earlier. We find that log m_{max} increases slightly with log M_{cloud}, with a slope of ~ 0.2, significantly less steep than found by Larson.[4] Specifically, log m_{max} increases from ~ 1.4 when log $M_{cloud} = 5.0$ to ~ 1.7 when log $M_{cloud} = 7.0$. Thus at log $M_{cloud} \approx 5.0$, where the cloud masses in Larson's sample meet ours, the values of log m_{max} in Larson's sample join smoothly to ours. Therefore, our estimates of m_{max}, M_*, and star formation efficiency based on IMF clusters appear consistent with Larson's work on less massive clouds at generally closer distances than those considered here.

[4] This trend is based on data for $M_{cloud} > 10^5\ M_\odot$ and therefore does not necessarily conflict with the absence of massive stars in clouds with $M_{cloud} < 10^5\ M_\odot$ described in § IV*f*.

d) Star Formation Efficiency

We estimate the star formation efficiency, SFE = $M_*/(M_* + M_{cloud})$, by combining the stellar mass value for each H II region associated with a cloud, in Tables 3 and 4, with the mass estimate of the cloud, in Table 2. The SFE is a key quantity in models of star formation and cloud evolution (e.g., Mathieu 1983) and is relatively insensitive to distance uncertainties. Each estimate of SFE has an estimated relative precision of a factor of ~ 4, on the following basis. The M_{cloud} has relative precision of a factor of ~ 3, due mainly to improper choices of clip threshold and cloud boundary. (Possible errors in the CO to hydrogen conversion, or in the decision to clip rather than to subtract the background, affect the accuracy but not the precision of each estimate, since each of these errors gives a nearly constant bias to M_{cloud}.) The M_* also has a relative precision of a factor of ~ 3, due to uncertainties in background subtraction. Thus the SFE has a relative precision of a factor of ~ 4, and a ratio $\gtrsim 20$ in SFE from one cloud to the next is probably significant. The relative accuracy of each estimate is harder to judge, but may be a factor of 3–10. If each local maximum in Figure 3 is considered a cloud, then the values of SFE will necessarily increase, by factors between 1 and 10. However, the relative range of SFE, and the overall SFE, $M_*/(M_* + M_{cloud})$, where M_* is the total stellar mass and M_{cloud} the total cloud mass in the inner Galaxy, remain essentially unchanged.

The calculated values of SFE are presented in Table 5 for each cloud. Although the absolute values are highly uncertain, the relative variation in SFE from ~ 0.5 for 43,11 (W49) to $\sim 6 \times 10^{-4}$ for 37,82 is significant and reflects a highly nonuniform distribution of stars from one cloud to the next. The median value of SFE = 0.02 in Table 5 is similar to the mean values obtained by calculating the total star mass and the total cloud mass in our sample and forming the appropriate ratios. We examined the values of SFE for evidence of regional variation but found no significant change either along the Sagittarius arm or as a function of galactocentric radius $4 \leq R \leq 10$ kpc.

VII. INTERPRETATION AND DISCUSSION

a) Comparison with Another CO Survey

The results presented here concerning CO clouds are based on CO observations made with coarser angular resolution and more complete sampling than that of some other CO surveys, and it is worthwhile to investigate whether these differences influence our conclusions. We compare our results with those from the SSS CO survey described by Sanders, Scoville, and Solomon (1985, hereafter SSS*b*) and Sanders, Solomon, and Scoville (1983, hereafter SSS*a*). This survey used angular resolution 1′, *l*-direction spacing 1°, *b*-direction spacing 12′ over an angular area $-4° \leq l \leq 70°$, $-2° \leq b \leq 2°$. Thus the SSS survey area includes that of the Cohen *et al.* (1980) survey; the SSS angular resolution is ~ 8 times finer than that of the

Cohen *et al.* survey; and the SSS survey covers $\sim 10^{-3}$ of its survey area within its FWHM beam contour, while the Cohen *et al.* survey covers ~ 0.4.

In the Cohen *et al.* survey area, SSS*b* find 255 local maxima in the *l-v* plane that they interpret as 255 individual clouds, whereas we find 52 features containing one or more local maxima in the *l-b* plane (Figs. 3 and 4) that we interpret as 54 individual clouds. Inspection of specific regions indicates that the ratio of cloud numbers, 255:54 $\approx$ 5:1, reflects no significant discrepancy between the data in the surveys, but rather a difference in interpretation as to what constitutes a cloud—a difference traceable to the differences in sampling and resolution between the surveys. For example, our cloud 17,22 (associated with M16) appears to agree in *l*, *b*, and *v* with, and to contain, the six features denoted by SSS*b* as 91, 92, 97, 98, 99, and 100. Our cloud 49,59 (associated with W51) agrees in *l*, *b*, and *v* with, and contains, the four features 338, 339, 343, and 344. Because of its coarser resolution and more complete sampling, the Cohen *et al.* survey appears better suited to the recognition of structures $\gtrsim 1°$ in extent than the SSS survey. Therefore the typical "cloud" in this paper contains ~ 5 "clouds" according to SSS*b* and can be considered a complex that contains smaller units. Similarly, one could consider each local maximum in Figure 3 to be a "cloud." In that case, there are about three "clouds" on average in each of the 54 objects studied here. The difference between the five SSS*b* "clouds" and the three local-maximum-on-Figure 3 "clouds" is probably due to the relatively finer angular resolution of the SSS*b* survey.

SSS*b* found that hotter clouds, as indicated by their peak CO intensity, are more frequently associated with H II regions than are cooler clouds. Analysis of the present data indicates a similar trend. In analogy with Figure 6 of SSS*b*, we have examined the number of H II regions associated with a cloud as a function of the peak CO emission contour in the cloud map. In each data set, there are a small number of H II regions per cloud (zero for SSS*b*, 0.6 for the present data) for the three lowest contour values. Then the number of H II regions per cloud increases steeply with increasing contour value, rising to a maximum of 0.9 for the SSS*b* data and to 5.0 for the present data. If, as suggested above, one considers each cloud in this paper to contain roughly 5 SSS*b* clouds, then the two trends are consistent within errors due to binning and quantization.

b) Comparison with Another Stellar Mass Distribution

The stellar mass estimates given here are based on a model mass distribution (the IMF) for which most of the model luminosity is observed (from massive stars) but little of the deduced stellar mass (from low-mass stars) contributes to the observed luminosity. An alternate model, which does not rely on extrapolation to unobserved stars, assigns the observed IRE and L_* to a large number of identical O stars (e.g., Odenwald and Fazio 1984). We have also used this model to deduce values of stellar mass and SFE. For the typical cloud, the identical–O-star model gives stellar mass and SFE about 15 times less than the IMF model. These O star values are much lower than those compiled by Larson (1982) for less massive clouds and yield values of SFE much lower than most estimates. Therefore, we consider the identical–O-star model as an unrealistic alternative to the IMF cluster model.

c) Variations in Stellar Content

The surveys compared here make possible for the first time the identification of massive ($M_{\rm cloud} > 10^6\ M_\odot$) molecular clouds having extremely few O stars. The absence of O stars in low-mass clouds is well known, but examples of massive clouds with few O stars have been rare because the earliest CO surveys were biased toward bright H II regions. There are 15 clouds in Table 5 having mass $10^6\ M_\odot$ or greater and having SFE ≤ 0.01. Of these, seven have no H II region emission at 5 GHz stronger than 1 Jy; the rest have detected emission $\lesssim 10$ Jy. Some of the clouds have questionable status because of uncertain boundaries (22,53), uncertain near/far assignment (23,78N and 23,78F), or large distance (27,25); but the following are probably genuine O-star–poor clouds: 29,80 (SFE = 0.001), 37,82 (<0.0006), 31,48 (<0.002), and the string of clouds in the Sgr arm 36,57 (0.003), 40,59 (0.002), 43,63 (0.006), and 44,60 (<0.005). Such massive, star-poor clouds are likely to be important in understanding factors that may be associated with O star formation. The low O star content of these clouds, and of those with $M < 10^5\ M_\odot$, suggest that cloud mass greater than $10^5\ M_\odot$ may be necessary but not sufficient for O star formation. It remains to be determined whether the absence of O stars in low-mass clouds can be attributed to an intrinsic difference between low- and high-mass clouds or simply to a lower likelihood of forming massive stars because there is less cloud mass available.

At the opposite extreme lie clouds having high star formation efficiency. There are ten clouds with SFE ≥ 0.04, of which four (20,25, 38,16, 49,18, and 54,40) may be questioned because of their relatively weak CO emission and far kinematic distance assignment, and two (17,44 and 25,55F) because of uncertain boundaries or near/far division. It appears more certain that 14,20 (M17; SFE = 0.04),17,22, (M16, 0.05), 43,11 (W49, 0.5), and 49,59 (W51, 0.04) are among the most O-star–rich clouds in the present sample. These clouds have SFE at least a factor of 20 greater than those discussed above. Why do inner Galaxy clouds vary so widely in production of luminous stars? Possibly relevant factors include the cloud mass, cloud age, the distribution of temperature and turbulence within the cloud, and the star-forming history of the cloud. Detailed studies are now warranted of gas properties of high- and low-mass clouds and of clouds rich and poor in O stars. It is also desirable to study O-star–poor clouds in the radio and infrared continuum for evidence of stars of type later than O.

The median value of SFE for the clouds in Table 5 is SFE = 0.02. The predictions of Mathieu (1983; 0.3–0.5) refer to the region of a cloud that produces a bound cluster. If one considers a single local maximum in Figure 3, containing a H II region/FIR source, then the median SFE increases by a factor of 3–5 to 0.06–0.1 (see § IV*a*). Mathieu's predicted SFE is greater still by a factor of 3–5, and the discrepancy might be explained in several ways. Perhaps the simplest explanation is that bound clusters are relatively rare among stellar groups, and few of the H II–FIR–CO peaks in Figure 3 are emerging bound clusters. Of the 68 H II regions in Table 2, five have reliable CO cloud associations and single–CO–maximum values SFE $\gtrsim 0.2$: 15.1 − 0.6 (M17), 16.4 − 0.3, 25.4 + 0.1 (W42), 43.1 + 0.1 (W49), and 48.6 + 0.0.

d) Cloud Density and Growth Time

The 54 CO clouds considered here are complexes in the sense that they have irregular shapes and many distinct peaks of emission. As discussed in § VII*a*, they typically contain several structures identified as individual clouds in SSS*b*. The close coincidence of many of these 54 clouds with H II regions and their approximate virial balance (Dame *et al.* 1985) support the idea that each cloud is generally a bound entity

and not a chance line-of-sight coincidence of smaller, unrelated clouds. These large clouds have much lower mean (volume-average) gas density n than the ~ 300 cm^{-3} needed to excite the CO transition because their complex, nonuniform structure implies a volume-filling factor much less than unity. The five most massive clouds in Table 2 have $n = 19$ cm^{-3} if each cloud is a uniform sphere of angular diameter $(\Delta l \Delta b)^{1/2}$, or $n = 16$ cm^{-3} if each cloud is a uniform cylinder of angular length Δl and diameter Δb. We therefore take $n = 18$ cm^{-3} as typical of the largest clouds in the inner Galaxy. The volume-filling factor is then $\lesssim 0.1$.

We use this mean density to estimate the characteristic growth times of these large clouds. We consider growth by accretion, due either to random collisions with smaller clouds or to gravitational attraction of surrounding gas. In either case, the rate of mass increase can be written

$$\dot{M} = 4\pi R^2 \mu n_{\rm ext} V , \tag{6}$$

where R is the (spherical) cloud radius, μ is the mean mass per particle, $n_{\rm ext}$ is the volume-average density of the gas accreting onto the cloud, and V is the speed of the accreting gas with respect to the cloud.

For random collisions we take $V \equiv V_{\rm col}$ to be a constant and find that the time to grow to mass M from $M/10$ is

$$\tau_{\rm col} = \frac{0.333(M/\mu)^{1/3} n^{2/3}}{n_{\rm ext} V_{\rm col}} . \tag{7}$$

We take $M = 5 \times 10^6\ M_\odot$, typical of the larger clouds described here, and $V_{\rm col} = 5$ km s^{-1} (Scoville and Hersh 1979). Then

$$\tau_{\rm col} = 2.90 \times 10^7 n^{2/3} n_{\rm ext}^{-1} \text{ yr} . \tag{8}$$

For gravitational accretion, we take the virial speed $V \equiv V_{\rm grav} = (GM/R)^{1/2}$. Then the time to grow to M from $M/10$ is

$$\tau_{\rm grav} = 2.35 \times 10^7 n^{1/2} n_{\rm ext}^{-1} \text{ yr} , \tag{9}$$

an expression similar to the free-fall time.

Equations (8) and (9) show that these two growth times are nearly equal and that the cloud age estimates based on accretive growth depend critically on n and $n_{\rm ext}$. Table 6 shows estimates of $\tau_{\rm col}$ and $\tau_{\rm grav}$ based on three pairs of values of n and $n_{\rm ext}$. Model A assumes $n = 300$ cm^{-3}, much higher than derived in this paper, but as expected for a CO cloud uniformly filled with emitting gas, and $n_{\rm ext} = 2$ cm^{-3}, as expected if CO clouds are much denser than their immediately surrounding gas. These numbers are similar to those adopted by Scoville and Hersh (1979) and Bash, Hausman, and Papaloizou (1981). Model B assumes $n = 18$ cm^{-3}, as derived from clouds in this paper; and $n_{\rm ext} = 2$ cm^{-3} as in A. Model C assumes $n = 18$ cm^{-3}, as in B, and that the gas surrounding each cloud is only slightly less dense, on average, than that in the cloud.

TABLE 6

ACCRETIVE GROWTH TIMES FOR THREE MODELS

Model	$n_{\rm ext}$ (cm^{-3})	n (cm^{-3})	$\tau_{\rm col}$[a] (yr)	$\tau_{\rm grav}$[a] (yr)
A.....	2	300	6.5×10^8	2.0×10^8
B.....	2	18	1.0×10^8	5.0×10^7
C.....	12	18	1.7×10^7	8.3×10^6

[a] $\tau_{\rm col}$ and $\tau_{\rm grav}$ are the times to grow by a factor of 10 in mass via random collisions and gravity respectively.

Specifically, model C assumes that $n(r) \propto r^{-1}$, so that $n_{\rm ext} = 2n/3$.

Table 6 shows that the growth time for collisional accretion is slightly greater than that for gravitational accretion, by a factor of a few; but the growth time for model A exceeds that for model C by a much bigger factor, ~ 25–50. Thus the choice among accretive growth models (e.g., Scoville and Hersh 1979; Kwan 1979; Cowie 1981; Elmegreen 1982) is probably less important than the realistic choice of density values. The values derived in this paper, in models B and C, give growth time $\sim 10^7$–10^8 yr, consistent with estimates by Bash, Green, and Peters (1977), Blitz and Shu (1980), and Cohen *et al.* (1980).

If each local maximum is considered a "cloud," then the procedure described above gives mean density $n \approx 70$ cm^{-3} rather than ~ 20 cm^{-3}, and the growth times in Table 6 change slightly (for model B, they increase by a factor of ~ 2; for model C, they decrease by a factor of ~ 2). The conclusions of this section remain unchanged.

e) *Star-forming History of Giant Clouds*

The estimates of star formation efficiency in § VI*d* have a bearing on the history of O star formation in giant clouds. We estimate the ratio $\tau_{\rm O}/\tau_{\rm any}$, in which $\tau_{\rm O}$ is the time interval over which the molecular clouds seen now in the inner Galaxy have been producing O stars, and $\tau_{\rm any}$ is the interval over which the same clouds have been producing stars of any type. The method of stellar mass estimation in § VI*d*, based on the IMF, assumes that all the O stars ever produced by the cloud are still in the cloud. We denote the corresponding estimates of the total stellar mass in clouds in the inner Galaxy and the star formation efficiency of these clouds as $M_*(1)$ and SFE(1). As noted in § VI*d*, a more correct estimate allows for the O stars that have left their parent clouds. In that case the stellar mass is $M_*(R) = RM_*(1)$, and we define the SFE as SFE(R), given by

$$\frac{1}{\rm SFE}(R) = 1 + \frac{1}{R}\left[\frac{1}{\rm SFE}(1) - 1\right] . \tag{10}$$

An estimate of R comes from

$$R = \tau_{\rm O}/\tau_{\rm O,\,in} , \tag{11}$$

where $\tau_{\rm O,\,in}$ is the mean time that an O star stays in its parent cloud and produces localized (as opposed to "diffuse") H II/FIR region emission. Smith, Biermann, and Mezger (1978) estimate that the typical O star spends 0.1 of its main-sequence life in this phase, so we take $\tau_{\rm O,\,in} \approx 4 \times 10^5$ yr.

The time-average rate of forming all stellar mass by molecular clouds now in the inner Galaxy, $\langle \dot{M}_* \rangle$, can be written

$$\langle \dot{M}_* \rangle = M_{\rm cloud} R[{\rm SFE}(1)^{-1} - 1]^{-1} \tau_{\rm any}^{-1} . \tag{12}$$

Here $M_{\rm cloud}$ is the total cloud mass seen now in the inner Galaxy, and $R[{\rm SFE}(1)^{-1} - 1]^{-1}$ is just $M_*(R)/M_{\rm cloud}$ expressed in a more convenient form. Combining equations (11) and (12) gives

$$\frac{\tau_{\rm O}}{\tau_{\rm any}} = \frac{\tau_{\rm O,\,in} \langle \dot{M}_* \rangle [{\rm SFE}(1)^{-1} - 1]}{M_{\rm cloud}} . \tag{13}$$

We evaluate this expression, which is independent of R, for the inner Galaxy, i.e., within the solar circle. For $M_{\rm cloud}$ we adopt $1 \times 10^9\ M_\odot$, based on results of this paper, of Dame (1984), Dame *et al.* (1985), and SSS*b*. For $\langle \dot{M}_* \rangle$ we adopt $10\ M_\odot$ yr^{-1}, based on the expectation that the inner Galaxy value

should be somewhat larger than the solar neighborhood value, averaged over the solar circle, of 2 $M_\odot$ yr^{-1} (Tinsley 1981), and on the inner Galaxy estimates of 13 $M_\odot$ yr^{-1} (Güsten and Mezger 1982) and 12 $M_\odot$ yr^{-1} (Rengarajan 1984). For SFE(1) we take 0.02, from § VI*a*.[5] In each of the four quantities in equation (13) we estimate a relative uncertainty of a factor of ~ 3. The resulting value is $\tau_O/\tau_{any} = 0.2$, uncertain by a factor of ~ 6. This suggests that O star formation in the present-day inner Galaxy clouds may be appreciably more recent than the formation of other stars.

By itself, this result must be considered speculative because of the relatively large uncertainty in τ_O/τ_{any}. It is consistent with a well-known picture where clouds form low-mass stars first, intermediate-mass stars next, and massive stars last (Herbig 1962; Iben and Talbot 1966; Larson 1982; Adams, Strom, and Strom 1984; Doom, De Greve, and de Loore 1985). However, the present result also appears consistent with the picture described by Elmegreen (1983), in which stars of every mass form at random times in a cloud's history and with frequency that decreases with increasing stellar mass. The most massive stars rarely form; but upon formation, they rapidly destroy the cloud, and thus form last.

A complementary approach to the present SFE analysis was taken by Rengarajan (1984). He used the same CO–based estimates of M_{cloud} as in this paper, but FIR data from GPS (40′ beam) rather than from Hauser *et al.* (1984) (10′ beam). Rengarajan thus obtained FIR luminosity estimates for each cloud rather than for each H II region in the cloud and noted a correlation between L_{FIR} and M_{cloud} consistent with $L_{FIR}/M_{cloud} \approx 6\ L_\odot/M_\odot$. He used this result to obtain 0.2–0.4 for the quantity referred to in this section as SFE(R). As noted in § VI*a*, the values of L_{FIR} from GPS are 3–10 times larger than those obtained here from Hauser *et al.* (1984). As suggested above, this discrepancy may be due mainly to differing angular resolution, rather than (say) errors in intensity calibration. Then there may be no significant inconsistency in combining SFE(1), based on FIR emission originating near H II regions, with SFE(R), based on FIR emission from cloud locations both near to and far from H II regions. If so, then equation (10) and the values for SFE(1) and SFE(R) described here give $R \approx 10$–30, whence equation (11) gives $\tau_O \approx 0.5$–2×10^6 yr, and equation (13) gives $\tau_{any} \approx 3$–10×10^7 yr.

Additional constraints on the star-forming ages τ_O and τ_{any} of the inner Galaxy cloud material follow from placing a plausible limit on the star formation efficiency. We adopt SFE(R) < 0.5, guided by results for local clouds that satisfy this limit (Cohen and Kuhi 1979; Myers 1982; Wilking and Lada 1983). Then, since SFE(1) = 0.02, $R < 49$. Then equation (11) implies $\tau_O < 2 \times 10^7$ yr, and equation (13) implies $\tau_{any} < 1 \times 10^8$ yr. The range of τ_O derived above and the limit derived here suggest that O stars have been forming for at most a few main-sequence lifetimes—and probably in many clouds O stars have been forming for only one main-sequence lifetime. Thus it seems possible that most O stars produced by the present-day inner Galaxy clouds are still on the main sequence.

If the growth time $\sim 10^7$ yr estimated in § VII*d* is correct, and if the inner Galaxy clouds began forming stars as soon as they themselves formed, then the cloud ages lie in the range 2–10×10^7 yr, consistent with estimates by Bash, Green, and Peters (1977), Blitz and Shu (1980), and Cohen *et al.* (1980), but lower than estimates by Scoville and Hersh (1979). This range allows the possibility that linear features such as the Sagittarius arm form on the passage of a Galactic density wave and disperse significantly before the arrival of the next such wave, $\sim 2 \times 10^8$ yr later. If the dispersal is due to the effects of O stars, then the age limits deduced here suggest that the O stars accomplish this dispersal in a remarkably short period—at most a few main-sequence lifetimes.

[5] Assuming the alternative cloud definition that each local maximum in Figure 3 is a "cloud" has no effect on the value SFE(1) = 0.02, since the total stellar mass and the total cloud mass are not influenced by the location or number of cloud-cloud boundaries.

VIII. SUMMARY AND CONCLUSIONS

In this paper we have analyzed and compared surveys of the Galaxy covering $12° \leq l \leq 60°$, $-1° \leq b \leq 1°$ in the 2.6 mm line of CO (Cohen *et al.* 1980), in the 150 and 250 μm continuum (Hauser *et al.* 1984), and in the 6 cm continuum (Altenhoff *et al.* 1970, 1978) and H 110α line (Downes *et al.* 1980), in order to study the degree of association between H II regions and molecular clouds and to estimate the stellar content of molecular clouds.

The 54 molecular clouds and their associated H II region/FIR sources are described in Table 2. Analysis of these data leads to the following conclusions:

1. Most of the FIR sources are associated with H II regions, and essentially all the H II regions are associated with molecular clouds. Clouds having no H II region tend to have lower mass than clouds with H II regions. The distribution of massive clouds in the Galactic plane appears consistent with previous results for H II regions; the Sagittarius arm is relatively well defined. There, the arm definition in terms of CO cloud emission is somewhat better than in terms of radio continuum emission.

2. FIR and Lyα luminosities of associated H II regions indicate a median infrared excess of 6, in agreement with most prior observations. We see no significant evidence for a decrease in infrared excess with increasing galactocentric radius. Typically, the FIR and Lyα luminosities of an H II region indicate the presence of $\sim 5 \times 10^4\ M_\odot$ of stellar mass, if the luminosities are due to identical clusters following the Miller-Scalo IMF, and if all the O stars ever produced by the cloud are still in the cloud. For the entire sample of clouds, the star formation efficiency (SFE) is then 0.02. Several massive ($M > 10^6\ M_\odot$) clouds have remarkably low SFE, SFE $\lesssim 10^{-3}$.

3. The stellar mass associated with a cloud shows a correlation with cloud mass of the form $M_* \propto M_{cloud}^{0.5 \pm 0.2}$, similar to that reported by Larson (1982) for less massive clouds. However, M_* has a much weaker correlation with the mass of the nearest single local maximum of CO emission.

4. The volume-averaged gas density in the largest inner Galaxy clouds is ~ 20 cm^{-3}, as expected if such clouds are nonuniform and have low ($\lesssim 0.1$) volume-filling fractions. Such density is consistent with accretion times 10^7–10^8 yr.

5. For giant clouds now in the inner Galaxy, comparison of the SFE based on IMF clusters with estimates of the star formation rate indicate that these clouds may have been forming O stars for only the most recent $\sim 20\%$ of their star-forming life, the latter period being 10^8 yr or less. If stars began forming in the giant clouds when the clouds formed, then the cloud ages are probably several times 10^7 yr—consistent with formation during passage of a Galactic density wave and dispersal before passage of the next wave.

We thank numerous colleagues for discussions and preprints. P. C. M. thanks G. Field and I. Shapiro for support at the Center for Astrophysics, and C. Barrett for excellent typing.

APPENDIX A

DESCRIPTION OF 54 INNER GALAXY CLOUDS

We briefly describe each of the 54 molecular clouds tabulated in Table 2 and depicted in Figures 3 and 7. The descriptions include prominent associated H II regions, the basis of the adopted distance, and the reasons for the choice of cloud boundary in uncertain cases.

12,45.—Associated with W33; the mass may be underestimated if there is significant emission at longitude below the 12° survey cutoff. Near distance determined by H_2CO absorption.

13,54.—Near distance determined by H_2CO.

14,20.—Associated with M17; near distance determined by H_2CO and optical spectroscopy.

14,39.—Near distance determined by H_2CO.

17,22.—Associated with M16; there may be significant emission beyond the survey latitude cutoff at $b = 1°$; near distance determined by H_2CO and optical spectroscopy.

17,44.—Near distance determined by latitude extent.

17,58.—Similar range of l as 17,44, but distinct from 17,44 on the l-v diagram. Near distance determined by latitude extent.

18,48.—Associated with RCW 166; near distance determined by H_2CO. Division between 18,48 and 20,42 is uncertain.

19,65.—Associated with W39; near distance determined by H_2CO.

20,25.—It is unclear whether this long string of weak emission is one complex or several unrelated objects. The choice of near distance is uncertain; it was made on the speculation that this region is associated with the nearby 17,22 (M16).

20,42.—Near distance determined by large negative latitude. Division between 20,42 and 18,48 uncertain.

21,60.—Associated with strong H II region; far distance determined by H_2CO; cloud is probably poorly resolved.

22,53.—A massive cloud with no H II regions or FIR sources; near distance determined by H_2CO.

23,78N and 23,78F.—Four associated H II regions have far distance determined by H_2CO, but as Dame *et al.* (1985) point out, substantial near-distance H_2CO absorption is also present, at almost the same velocity. Like Dame *et al.*, we attribute half the integrated intensity to 23,78N and half to 23,78F.

24,42.—This cloud appears more distinct on the l-v diagram from 25,53 than does 22,53 − from 22,53, so we consider it a separate cloud. The near distance is inferred from the latitude extent. The H II region 25.3 + 0.3 appears associated on the basis of its H 110α velocity, but is unusual in its displacement from the high-intensity contours. The weak, extended emission near (l, b) = (26°, 1°) may be an unrelated, more local object.

24,98.—This large, elongated cloud is associated with seven H II regions, all near the terminal velocity. The near distance was chosen, somewhat arbitrarily, as in Dame *et al.* (1985), Lockman (1979), and Georgelin and Georgelin (1976). The cloud appears as one complex feature in Figure 3*a*, but as two features on the l-v diagram, and because of its location near the tangent of the 4 kpc arm it is more likely to be a composite of separate clouds than are some of the other features. The division between this cloud and 31,95 is very uncertain. The associated H II regions are remarkable in that they all have similar 6 cm flux density.

24,110.—Distance corresponds to tangent velocity.

25,55N and 25,55F.—The powerful H II region W42 appears associated with this feature and is assigned the far distance by virtue of its H_2CO absorption. But as Dame *et al.* (1985) point out, the latitude extent of the emission makes it unlikely that all the emission is at the far distance. We follow Dame *et al.* and assign 25% of the integrated emission to the far distance and 75% to the near distance.

26,65.—Near distance determined by large negative latitude.

27,25.—Far distance determined by small angular size and small latitude; uncertain.

27,34.—This string of small-angle, low-latitude clouds appears associated with three H II regions, one having the far distance determined by H_2CO absorption, and two having a less certain far distance assignment.

29,52.—In Figure 3*a* this cloud has about the same position as 29,80, but the two are distinct in the l-v diagram. The near kinematic distance is implied by both H_2CO absorption and the large negative latitude.

29,80.—Near distance determined by H_2CO absorption. This remarkable cloud is one of the more massive in the survey, yet it has negligible H II region or FIR emission.

31,12.—Near distance determined by latitude; uncertain.

31,48.—A string of low-latitude clouds similar to 27,34, but with stronger CO emission and no H II regions. Far distance based on low latitude.

31,95.—Like 24,98, this appears as a nearly continuous feature in Figure 3*a*; but it has irregular structure in the l-v diagram. It may be plausible to subdivide the cloud at ∼29° and at ∼32.5°. The most intense CO emission appears associated with the powerful H II region W43, whose H_2CO absorption indicates the near distance.

33,10.—This extremely weak emission feature was classified because it appears close in angle and velocity to the H II region 32.8 + 0.3, thought from H_2CO absorption to be at the far distance. The association is highly uncertain.

35,13.—This weak, extended emission coincides with visible obscuration (No. 617 in the catalog of Lynds 1962) and H_2CO absorption (Myers 1973), both indicating the near distance.

35,44.—One of the major features in the CO l-v diagram of the first quadrant: a massive molecular cloud with large internal motions, straddling the 50 km s^{-1} boundary between the second and third panels in Figure 3*a*. It is associated with the supernova remnant W44 and nearby H II regions, whose H_2CO absorption indicates the near distance. The boundary between 35,44+ and 36,57 is somewhat uncertain.

36,57.—This feature appears on the l-v diagram as a relatively weak extension of the emission from 35,45 to higher longitude and

higher velocity. However, its low latitude and its closeness in angle and velocity to the far-distance H II region 37.4+0.0 suggest the far kinematic distance.

37,82.—This elongated feature appears as a single, large, relatively weak feature on the *l-v* diagram. Dame *et al.* (1985) and Dame (1984) call it the "Aquila spur" and suggest that it lies between the Sagittarius and Scutum arms, at the far distance of 9.5 kpc.

38,16, 39,32, and 39,42.—These weak, extended clouds are prominent on the *l-v* diagram and resemble 35,13. Their latitude extents indicate the near distance for each cloud. The association claimed here between 38,16 and the H II region 39.3+0.0 may be questioned, since the H II region distance ambiguity is not resolved.

40,59.—Associated with the far H II region 37.9−04 and concentrated toward the plane; far distance.

41,37.—Distinct on *l-v* diagram; large latitude extent indicates near distance.

42,16.—Concentration toward plane and apparent association with H II region 41.5+0.0, at $b = 0°$, suggest far distance.

43,11.—Associated with the very powerful far H II region W49.

43,63 and 44,60.—These two clouds, distinct on both Figure 3*b* and the *l-v* diagram, have uncertain distance. Their relatively large latitude extents imply a linear extent ~150 pc at the far distance and ~70 pc at the near distance. However, the latitude extents are about the same as that of the nearby (in angle and velocity) cloud 46,59, whose associated H II regions 45.1+0.1 and 45.5+0.1 have the far distance (10 kpc) implied by H_2CO absorption. We adopt the far distance for each object.

46,25.—This weak, extended feature is prominent on the *l-v* diagram. Its latitude extent suggests the near distance.

46,59.—see 43,63 and 44,60.

49,18.—This feature is distinct on the *l-v* diagram, is concentrated toward the plane like 43,11 (W49), and is associated with the far H II region 48.6+0.0; hence we adopt the far distance.

49,59.—W51 complex. The near distance is implied by the H_2CO absorption of three powerful associated H II regions and also by the proper motion of H_2O masers (Schneps *et al.* 1981).

50,45.—Near distance determined by latitude extent.

51,55 and 53,60.—These appear nearly continuous on Figure 3*b* but more distinct in the *l-v* diagram. Their large latitude extent indicates the near distance. These correspond to the single cloud 52,59 in Dame *et al.* (1985).

53,24.—Large angular extent implies near distance.

54,40, 56,36, and 58,37.—On the *l-v* diagram 54,40 and 56,36 appear single and distinct, while the feature called 58,37 appears as a closely spaced double, distinct from 56,36. For 54,40, the small angular size and concentration toward the plane indicate the far distance. For 56,36 and 58,37 the larger extents suggest the near distance.

60,27.—The large extent implies the near distance.

APPENDIX B

REMOVAL OF A SOURCE BACKGROUND BY CLIPPING AND SUBTRACTION

We show that the integrated intensity of an optically thin source, seen with an extended background, is better estimated by subtraction than by clipping; whereas the intensity of a thick source is better estimated by clipping if it lies in front of the background cloud, or by subtraction if it lies behind the background cloud. These considerations support the subtraction of an optically thin FIR background to estimate integrated source intensity.

We consider an idealized source of angular area Ω_s, with source function B_s, optical depth τ_s, and specific intensity I_s, each uniformly greater than zero over Ω_s and zero beyond. Then $I_s = B_s(1 - e^{-\tau_s})$, and the integrated intensity is $W_s = I_s\Omega_s$. The background cloud includes the source in projection, has angular area $\Omega_b \gg \Omega_s$, and has B_b, τ_b, I_b, and W_b defined as for the source. The observed on-source intensity is I_{on}; the observed off-source (and on-background) intensity is $I_{off} = I_b$; we denote I_{on}/I_{off} as u, and require $u > 1$ for recognition of the source as a source. The clipped estimate of W_s, W_{clip}, is obtained by replacing the observed intensity I by zero when $0 \le I \le I_{off}$. The subtracted estimate of W_s, W_{sub}, is obtained by replacing I by $I - I_{off}$ when $I \ge I_{off}$. We denote the relative accuracy of estimating W_s by W_{clip} as

$$\Delta_{clip} \equiv \frac{W_{clip} - W_s}{W_s} \tag{B1}$$

and the relative accuracy of estimating W_s by W_{sub} as

$$\Delta_{sub} \equiv \frac{W_{sub} - W_s}{W_s} . \tag{B2}$$

When the source is in front of the background cloud, the equation of radiative transfer may be combined with the definitions above to give

$$\Delta_{clip} = (ue^{\tau_s} - 1)^{-1} , \tag{B3}$$

$$\Delta_{sub} = -(e^{\tau_s} - 1)/(ue^{\tau_s} - 1) . \tag{B4}$$

For a thin source, $\tau_s \ll 1$,

$$\Delta_{clip} \approx (u - 1)^{-1} , \tag{B5}$$

$$\Delta_{sub} \approx -\tau_s(u - 1)^{-1} , \tag{B6}$$

and for the case of interest here where $u \approx 3$, $\Delta_{\rm clip}$ is of order unity while $\Delta_{\rm sub}$ is much less than unity. For a thick source, $\tau_s \gg 1$,

$$\Delta_{\rm clip} \approx (ue^{\tau_s})^{-1} , \tag{B7}$$

$$\Delta_{\rm sub} \approx -u^{-1} , \tag{B8}$$

and $\Delta_{\rm sub}$ is of order unity while $\Delta_{\rm clip}$ is much less than unity.

When the source is behind the "background" cloud, its optical depth is unimportant, but the "background" optical depth τ_b matters. The case $\tau_b \gg 1$ is not of interest, since the source would not be visible. For $\tau_b \ll 1$,

$$\Delta_{\rm clip} \approx -\tau_b + (u-1)^{-1} , \tag{B9}$$

$$\Delta_{\rm sub} \approx -\tau_b , \tag{B10}$$

and $\Delta_{\rm clip}$ is of order unity while $\Delta_{\rm sub}$ is much less than unity.

These relations (B5)–(B10) can be summarized according to the source optical depth. If the source is thin, subtraction is significantly more accurate than clipping, independent of source location, and gives relative accuracy of order τ_s (source in front) or τ_b (source in back). If the source is thick, the choice depends on source location: clipping is more accurate if the source is in front, while subtraction is more accurate if the source is in back. Since one may not know the relative location of the source and the background cloud, this thick-source case is more ambiguous than the thin-source case. If one makes the "wrong" choice of procedure, one introduces a relative error of order unity, either upward (source in back, clipped) or downward (source in front, subtracted).

This analysis assumes that the source emission profile has a step-function change in intensity between $I_{\rm on}$ and $I_{\rm off}$, so that errors in estimating source size are unimportant. When the on-source intensity decreases gradually into the background, source-size errors complicate the analysis given above. Briefly, a model of source intensity versus position gives the relative error in $W_{\rm sub}$ due to an error in I_b as proportional to $(1-u)^{-3}$, while the relative error in $W_{\rm clip}$ due to the same error in I_b is proportional to $(1-u)^{-2}$. These results suggest that clipping and subtraction give similar errors in W due to an error in I_b when the source is much stronger than the background, but that subtraction gives a significantly bigger error than does clipping when the source is only slightly stronger than the background.

These considerations are referred to in §§ IV*b* amd V*a* and in Appendix C.

APPENDIX C

COMPUTATION OF FIR LUMINOSITY

To compute the FIR luminosity associated with each source, we first estimated a 150 μm background flux level for each source. This background level was (1) the two-dimensional local minimum of intensity whose (l, b)-position is nearest to that of source peak; or (2), when the source lies on a ridge, narrow in b and long in l, the nearest local minimum in the l-direction; or (3), when no significant minimum was nearby, the average intensity of the surrounding plateau. We made a large-scale contour map of the 150 μm emission around each source and identified a background value by direct inspection or by taking a cut, usually through the peak of the source in the l-direction. This procedure is somewhat subjective; a variation of $\sim 30\%$ may occur among background choices made according to the above guidelines, for a given source. This uncertainty is probably similar to or greater than that arising from subtraction of a background that is constant over the source, as opposed to a background that more closely follows the slope of the Galactic ridge at the source location.

We then obtained the total FIR luminosity by the following steps: (1) We inspected the longer wavelength (250 μm) map to see whether a significant "source" is present at the same location. (2) If so, we measured the peak fluxes $p(150)$ and $p(250)$ and obtained the background fluxes $b(150)$ and $b(250)$ as described above. (3) Then we subtracted the 150 μm background from the 150 μm map, and computed $F_{\rm int}(150)$, the integrated 150 μm flux above background. (4) We obtained $F_{\rm int}(250)$ by assuming that the source has essentially the same projected size and shape at 250 μm as at 150 μm and differs only in relative intensity; then

$$F_{\rm int}(250) = F_{\rm int}(150)\,\frac{p(250)-b(250)}{p(150)-b(150)} . \tag{C1}$$

This step generally gave less variable results than the possible alternative of subtracting the 250 μm background from the 250 μm map and then integrating, perhaps because the 250 μm map has relatively poor signal-to-noise ratio for weak sources. (5) The ratio $F_{\rm int}(150)/F_{\rm int}(250)$ was compared to model ratios of blackbody functions, each function integrated over the corresponding instrumental passband and weighted by emissivity proportional to λ^{-2}, as in Hauser *et al.* (1984), for a range of color temperatures. Graphs of the passbands are given in Cheung (1980). Thus the color temperature T and total FIR flux $F_{\rm FIR}$ are obtained. (6) Then the far-infrared luminosity $L_{\rm FIR}$ was calculated from $L_{\rm FIR} = 4\pi D^2 F_{\rm FIR}$, where D is the distance assigned to the corresponding molecular cloud, column (4) of Table 2.

REFERENCES

Adams, M., Strom, K., and Strom, S. 1984, *Ap. J.*, submitted.
Altenhoff, W., Downes, D., Goad, L., Maxwell, A., and Rinehart, R. 1970, *Astr. Ap. Suppl.*, **1**, 319.
Altenhoff, W., Downes, D., Pauls, T., and Schraml, J. 1978, *Astr. Ap. Suppl.*, **35**, 23.
Bash, F., Green, E., and Peters, W. 1977, *Ap. J.*, **217**, 464.
Bash, F., Hausman, M., and Papaloizou, J. 1981, *Ap. J.*, **245**, 92.
Bisiacchi, G., Firmani, C., and Sarmiento, A. 1983, *Astr. Ap.*, **119**, 167.
Blitz, L., Fich, M., and Stark, A. 1982, *Ap. J. Suppl.*, **49**, 183.
Blitz, L., and Shu, F. 1980, *Ap. J.*, **238**, 148.

Boissé, P., Gispert, R., Coron, N., Wijnbergen, J., Serra, G., Ryter, C., and Puget, J. 1981, *Astr. Ap.*, **94**, 265.
Burton, W. 1971, *Astr. Ap.*, **10**, 76.
Cheung, L. 1980, Ph.D. thesis, University of Maryland (NASA Tech. Memorandum, No. 82056).
Cohen, M., and Kuhi, L. 1979, *Ap. J. Suppl.*, **41**, 743.
Cohen, R., Cong, H., Dame, T., and Thaddeus, P. 1980, *Ap. J.* (*Letters*), **239**, L53.
Cohen, R., Dame, T., and Thaddeus, P. 1985, *Ap. J.*, submitted.
Cowie, L. 1981, *Ap. J.*, **245**, 66.
Dame, T. 1984, NASA Tech. Paper No. 2288.
Dame, T., Elmegreen, B., Cohen, R., and Thaddeus, P. 1985, *Ap. J.*, submitted.
Doom, C., De Greve, J., and de Loore, C. 1985, *Ap. J.*, **290**, 185.
Downes, D., Wilson, T., Bieging, J., and Wink, J. 1980, *Astr. Ap. Suppl.*, **40**, 379.
Elmegreen, B. 1982, *Ap. J.*, **253**, 655.
———. 1983, *M.N.R.A.S.*, **203**, 1011.
Garmany, C., Conti, P., and Chiosi, C. 1982, *Ap. J.*, **263**, 777.
Georgelin, Y. M., and Georgelin, Y. P. 1976, *Astr. Ap.*, **49**, 57.
Gispert, R., Puget, J., and Serra, G. 1982, *Astr. Ap.*, **106**, 293 (GPS).
Güsten, R., and Mezger, P. 1982, *Vistas Astr.*, **26**, 159.
Hauser, M., *et al.* 1984, *Ap. J.*, **285**, 74.
Herbig, G. 1962, *Adv. Astr. Ap.*, **1**, 47.
Ho, P., and Haschick, A. 1981, *Ap. J.*, **246**, 761.
Iben, I., and Talbot, R. 1966, *Ap. J.*, **144**, 968.
Israel, F. 1978, *Astr. Ap.*, **70**, 769.
Jaffe, D., Stier, M., and Fazio, G. 1982, *Ap. J.*, **252**, 601.
Kwan, J. 1979, *Ap. J.*, **229**, 567.
Larson, R. 1982, *M.N.R.A.S.*, **200**, 159.
Lebrun, F., *et al.* 1983, *Ap. J.*, **266**, 276.
Liszt, H. 1982, *Ap. J.*, **262**, 198.
Lockman, F. 1979, *Ap. J.*, **232**, 761.
Lynds, B. 1962, *Ap. J. Suppl.*, **7**, 1.
Mathieu, R. 1983, *Ap. J.* (*Letters*), **267**, L97.
McBreen, B., Fazio, G., and Jaffe, D. 1982, *Ap. J.*, **254**, 126.
Mezger, P. 1978, *Astr. Ap.*, **70**, 565.
Mezger, P., Smith, L., and Churchwell, E. 1974, *Astr. Ap.*, **32**, 269.
Miller, G., and Scalo, J. 1979, *Ap. J. Suppl.*, **41**, 513.
Myers, P. 1973, *Ap. J. Suppl.*, **229**, 26.
———. 1977, *Ap. J.*, **211**, 737.
———. 1982, *Ap. J.*, **257**, 620.
Odenwald, S., and Fazio, G. 1984, *Ap. J.*, **283**, 601.
Okuda, H. 1981, in *IAU Symposium 96, Infrared Astronomy*, ed. C. Wynn-Williams and D. Cruikshank (Dordrecht: Reidel), p. 247.
Panagia, N. 1983, *Ap. J.*, **78**, 929.
———. 1974, *Ap. J.*, **192**, 221.
Petrosian, V., Silk, J., and Field, G. 1972, *Ap. J.* (*Letters*), **177**, L69.
Reifenstein, E., Wilson, T., Burke, B., Mezger, P., and Altenhoff, W. 1970, *Astr. Ap.*, **4**, 357.
Rengarajan, T. 1984, *Ap. J.*, **287**, 671.
Rivolo, A., Solomon, P., and Sanders, D. 1985, *Ap. J.*, submitted.
Sanders, D., Scoville, N., and Solomon, P. 1985, *Ap. J.*, **289**, 373 (SSS*b*).
Sanders, D., Solomon, P., and Scoville, N. 1983, *Ap. J.*, **276**, 182 (SSS*a*).
Schmidt, M. 1965, in *Stars and Stellar Systems*, Vol. **5**, *Galactic Structure*, ed. A. Blaauw and M. Schmidt (Chicago: University of Chicago Press), p. 513.
Schneps, M., Lane, A., Downes, D., Moran, J., Genzel, R., and Reid, M. 1981, *Ap. J.*, **249**, 124.
Scoville, N., and Hersh, K. 1979, *Ap. J.*, **229**, 578.
Siegel, S. 1956, *Nonparametric Statistics for the Behavioral Sciences* (New York: McGraw-Hill), p. 127.
Smith, L., Biermann, P., and Mezger, P. 1978, *Astr. Ap.*, **66**, 65.
Solomon, P., Sanders, D., and Rivolo, A. 1985, *Ap. J.* (*Letters*), **292**, L19.
Tielens, X., and de Jong, T. 1979, *Astr. Ap.*, **75**, 326.
Tinsley, B. 1981, *Ap. J.*, **250**, 758.
Wilking, B., and Lada, C. 1983, *Ap. J.*, **274**, 698.

RICHARD S. COHEN, THOMAS M. DAME, and PATRICK THADDEUS: NASA/Goddard Institute for Space Studies, 2880 Broadway, New York, NY 10025

ELI DWEK, MICHAEL G. HAUSER, and ROBERT F. SILVERBERG: NASA/Goddard Space Flight Center, Code 693.2, Greenbelt, MD 20071

PHILIP C. MYERS: Center for Astrophysics, Mail Stop 42, 60 Garden Street, Cambridge, MA 02138